

# Abstract

The existence of invariant subspaces for bounded linear operators acting on an infinite-dimensional Hilbert space appears to be one of the most difficult questions in the theory of linear transformations. The question is known as the *invariant subspace problem*. Very few affirmative answers are known regarding this problem. One of the most prominent ones is the theorem on the existence of hyper-invariant subspaces for compact operators due to V.I. Lomonosov.

The aim of this work is to generalize Lomonosov's techniques in order to apply them to a wider class of not necessarily compact operators. We start by establishing a connection between the existence of invariant subspaces and density of what we define as the associated Lomonosov space in a certain function space. On a Hilbert space approximation with Lomonosov functions results in an extended version of Burnside's Theorem. An application of this theorem to the algebra generated by an essentially self-adjoint operator  $A$  yields the existence of vector states on the space of all polynomials restricted to the essential spectrum of  $A$ . Finally, the invariant subspace problem for compact perturbations of self-adjoint operators is translated into an extreme problem and the solution is obtained upon differentiating certain real-valued functions at their extreme.

The invariant subspace theorem for essentially self-adjoint operators acting on an infinite-dimensional real Hilbert space is the main result of this work and represents an extension of the known techniques in the theory of invariant subspaces.

EXPERIMENTAL EVIDENCE FOR ANOMALOUS MAGNETISM IN THE  
SUPERCONDUCTING STATE OF  $\text{YBa}_2\text{Cu}_3\text{O}_{6+x}$

By  
Roger I. Miller

A THESIS SUBMITTED IN PARTIAL FULFILLMENT OF  
THE REQUIREMENTS FOR THE DEGREE OF  
DOCTOR OF PHILOSOPHY

IN  
THE FACULTY OF GRADUATE STUDIES  
PHYSICS & ASTRONOMY

WE ACCEPT THIS THESIS AS CONFORMING  
TO THE REQUIRED STANDARD

.....  
.....  
.....  
.....

The University of British Columbia  
2002

© ROGER I. MILLER, JANUARY 2002

EXPERIMENTAL EVIDENCE FOR ANOMALOUS MAGNETISM IN THE  
SUPERCONDUCTING STATE OF  $\text{YBa}_2\text{Cu}_3\text{O}_{6+x}$

By  
Roger I. Miller

A THESIS SUBMITTED IN PARTIAL FULFILLMENT OF  
THE REQUIREMENTS FOR THE DEGREE OF  
DOCTOR OF PHILOSOPHY

IN  
THE FACULTY OF GRADUATE STUDIES  
PHYSICS & ASTRONOMY

WE ACCEPT THIS THESIS AS CONFORMING  
TO THE REQUIRED STANDARD

.....  
.....  
.....  
.....

The University of British Columbia

2002

© ROGER I. MILLER, JANUARY 2002

In presenting this thesis in partial fulfilment of the requirements for an advanced degree at the University of British Columbia, I agree that the Library shall make it freely available for reference and study. I further agree that permission for extensive copying of this thesis for scholarly purposes may be granted by the head of my department or by his or her representatives. It is understood that copying or publication of this thesis for financial gain shall not be allowed without my written permission.

---

Physics & Astronomy  
The University of British Columbia  
6224 Agricultural Road  
Vancouver, Canada  
V6T 1W5

Date:

---

*To grad students*

# Table of Contents

Abstract	1
Table of Contents	iii
List of Tables	v
List of Figures	vi
Acknowledgements	xi
<b>1 Introduction</b>	<b>1</b>
<b>2 YBa<sub>2</sub>Cu<sub>3</sub>O<sub>6+x</sub></b>	<b>4</b>
2.1 Chemical Structure of YBa <sub>2</sub> Cu <sub>3</sub> O <sub>6+x</sub> . . . . .	4
2.2 Evolution of behaviour with doping . . . . .	6
2.3 Magnetic behaviour in Zero Field . . . . .	9
2.3.1 $\mu^+$ SR measurements . . . . .	10
2.3.2 Neutron Measurements . . . . .	11
2.4 Magnetic behaviour in an applied field . . . . .	13
2.4.1 Magnetism induced by the Vortex State . . . . .	14
2.4.2 Evolution of the Vortex Lattice with Temperature and Magnetic Field . . . . .	15
<b>3 Theory</b>	<b>20</b>
3.1 Superconductors and the Vortex State . . . . .	20
3.1.1 The London Model . . . . .	21
3.1.2 The Ginzburg-Landau Model . . . . .	22
3.1.3 Non-local Effects, Microscopic Models, and <i>d</i> -wave symmetry .	22
3.1.4 Vortex Lattice States . . . . .	24

3.2	Anomalous Magnetism and Superconductors . . . . .	28
3.2.1	Spin Antiferromagnetism . . . . .	29
3.2.2	Orbital Antiferromagnetism . . . . .	30
3.3	Evolution of $\text{Cu}^{2+}$ spin magnetism with hole doping . . . . .	31
3.4	Conclusion . . . . .	32
<b>4</b>	<b>Experimental Methods</b>	<b>33</b>
4.1	SQUID Magnetometry . . . . .	33
4.2	$\mu^+$ SR measurements . . . . .	36
4.2.1	Transverse Field $\mu^+$ SR . . . . .	40
4.2.2	Zero Field $\mu^+$ SR . . . . .	42
4.3	Elastic Neutron Scattering . . . . .	44
4.3.1	Experimental Set up . . . . .	45
4.3.2	Magnetic neutron scattering . . . . .	45
<b>5</b>	<b>Results</b>	<b>48</b>
5.1	A phase diagram of the vortex state for Ortho-II $\text{YBa}_2\text{Cu}_3\text{O}_{6.50}$ . . . . .	48
5.1.1	Squid measurements of the irreversibility line . . . . .	49
5.2	Vortex State magnetism in $\text{YBa}_2\text{Cu}_3\text{O}_{6.50}$ . . . . .	53
5.2.1	$\mu^+$ SR evidence for vortex core magnetism in Ortho II $\text{YBa}_2\text{Cu}_3\text{O}_{6.50}$ . . . . .	53
5.2.2	Elastic neutron scattering in Ortho-II $\text{YBa}_2\text{Cu}_3\text{O}_{6.50}$ . . . . .	59
5.2.3	Conclusion . . . . .	61
5.3	The groundstate in Ortho-II $\text{YBa}_2\text{Cu}_3\text{O}_{6.35}$ . . . . .	64
5.3.1	Superconductivity in $\text{YBa}_2\text{Cu}_3\text{O}_{6.35}$ . . . . .	64
5.3.2	Antiferromagnetism in $\text{YBa}_2\text{Cu}_3\text{O}_{6.35}$ . . . . .	64
5.3.3	Conclusion . . . . .	71
<b>6</b>	<b>Discussion</b>	<b>72</b>
6.1	Vortex Core Magnetism . . . . .	72
6.2	Magnetism in $\text{YBa}_2\text{Cu}_3\text{O}_{6.35}$ . . . . .	74
6.3	Conclusion . . . . .	77
	<b>Bibliography</b>	<b>79</b>

# List of Tables

5.1	datasum . . . . .	67
6.1	Model of random disorder and stripes. . . . .	75

# List of Figures

2.1	Structure of $\text{YBa}_2\text{Cu}_3\text{O}_{6+x}$ . The $\text{Cu}^{2+}$ spins in the Cu-O planes are shown with red arrows. The chains here are shown with oxygen between the Cu chain ions. Both the superconductivity and antiferromagnetism occur in the Cu-O planes. . . . .	5
2.2	Possible phase diagrams near the AF/SC boundary ( $p = 0.05$ ) in clean, homogeneous crystals. Panel (a): coexistent SC and AF over a range of hole doping, possibly indicating competition between the two; panel (b) no coexistence between AF and SC at non-zero temperatures; panel (c) a transition at non-zero temperature to a state characterized by coexistent AF and SC. . . . .	8
2.3	$T_N$ 's and $T_c$ 's taken from various $\mu^+$ SR and neutron experiments in $\text{YBa}_2\text{Cu}_3\text{O}_{6+x}$ . Notice that all experimental data agrees with a large decrease in $T_N$ and $T_c$ near $x = 0.3 - 0.4$ . . . . .	12
3.1	The displacement correlation function grows linearly below $R_l$ and logarithmically above $R_a$ in the Bragg Glass phase of the vortex state. Inset: $C(r) = e^{G_0 u(r)}$ versus $r$ , showing the algebraic decay in the Bragg Glass model. . . . .	27
4.1	SQUID signal <i>vs</i> position in the pick up coil in $\text{YBa}_2\text{Cu}_3\text{O}_{6.50}$ at $T = 15.5$ K. The asymmetric tail about the center (25 a.u.) is a signal of pinning in the sample. The pinning is greatest in the zero field cooled (ZFC) run compared to the field cooled (FC) run. . . . .	34

4.2	Field cooled SQUID signal <i>vs</i> position in $\text{YBa}_2\text{Cu}_3\text{O}_{6.50}$ Flux creep during the measurement can yield a sloping background. . . . .	35
4.3	Schematic of experimental set up for 4 positron counters (dark boxes) surrounding sample (circle). Here the muon beam and applied magnetic field points into the page. The muon spin (straight arrow) precesses around the magnetic field at the Lamor frequency, sweeping by each of the counters. . . . .	37
4.4	Raw counts in a single counter as a function of time, at early times, for $\text{YBa}_2\text{Cu}_3\text{O}_{6.50}$ The oscillations are due to the precession of the muon spin polarization in a magnetic field of $\mu_0 H = 1$ T. The large number of data points in high fields makes the fitting of data in the “lab” frame very time intensive. Hence, transformations to a rotating reference frame at a frequency slightly below the main frequency of the superconductor is performed. . . . .	38
4.5	Raw counts in a single positron counter as a function of time for $\text{YBa}_2\text{Cu}_3\text{O}_{6.50}$ $\mu_0 H = 1$ T and $T = 2.5$ K. The oscillations at early time are binned over by selecting a time bin size larger than the oscillation period in a 1 Tesla field. . . . .	39
4.6	Muon polarization signal in $\text{YBa}_2\text{Cu}_3\text{O}_{6.50}$ in a magnetic field of $\mu_0 H = 1$ T in (a) the normal state and (b) the superconducting state ( $T = 2.5$ K). The small damping in the normal state is caused by the presence of randomly oriented nuclear spins. The additional damping in the superconducting state is primarily due to the broad magnetic field distribution of the vortex lattice. . . . .	41
4.7	Muon asymmetry signal in GE varnished $\text{YBa}_2\text{Cu}_3\text{O}_{6.00}$ at $T = 3$ K. The main signal precesses at a frequency proportional to 300 G due to the antiferromagnetically aligned $\text{Cu}^{2+}$ spins in the Cu-O planes. . . . .	43

4.8	Schematic of experimental set up for elastic neutron scattering. The angle between the sample-monochromator and neutron source-monochromator selects neutron energies and $k_i$ , the initial momentum. The analyzer rotates about the sample to choose different $k_f$ , the final neutron momentum. The angle made between the analyzer and detector is fixed for elastic scattering. The sample is mounted in a 4 K He cooled cryostat, surrounded by a 2.6 T split coil magnet. . . . .	44
5.1	Zero field cooled and field cooled magnetization measurements in $\text{YBa}_2\text{Cu}_3\text{O}_{6.50}$ in a magnetic field of $\mu_0 H = 4$ T perpendicular to the $a - b$ planes. The two signals differ below $T_{irr} = 15$ K and show evidence for a small peak near $T_{peak} = 20$ K. . . . .	50
5.2	Fitting parameter of ZFC and FC magnetization data in an applied field of $\mu_0 H = 4$ T in $\text{YBa}_2\text{Cu}_3\text{O}_{6.50}$ . A good fit is obtained for a fitting parameter $R=1$ . The onset of the decrease in $R$ near $T = 22$ K signals the beginning of the irreversible state. . . . .	51
5.3	Irreversibility line measured from magnetization in $\text{YBa}_2\text{Cu}_3\text{O}_{6.50}$ . $T_{onset}$ signals the decrease in the fitting parameter to the raw SQUID data; $T_{peak}$ corresponds to a peak in the ZFC and FC magnetization data; and $T_{irr}$ occurs where the ZFC and FC magnetization data clearly diverge. . . . .	52

5.4	Magnetic field distribution $n(B)$ in superconductors in an applied field of $H=4$ T, with and without vortex core alternating fields. Solid line: $n(B)$ calculated from Eq. 5.2.1 with alternating fields in the vortex cores ( $M = 15$ G); dashed line: field distribution without alternating fields calculated from Eq. 3.1.4 with identical values for $\xi$ and $\lambda$ . Notice that significant changes occur only in the high field tail. See text for further details. Inset: $B(r)$ along a line between two vortex cores. The solid line shows $B(r)$ without alternating fields, whereas the squares show $B(r)$ with $M=15$ G AF fields in the vortex core. The magnitude of the alternating fields decays away from the vortex core center. . . . .	54
5.5	Improvement in $\chi^2$ by varying $M$ of fits to muon polarization signal using Eqs. 5.2.1 and 4.2.1 in (a) $\text{YBa}_2\text{Cu}_3\text{O}_{6.50}$ (b) $\text{NbSe}_2$ (c) $\text{YBa}_2\text{Cu}_3\text{O}_{6.95}$ $\xi_{ab}$ in each panel is fixed at its $M=0$ value. . . . .	56
5.6	(a) Fast Fourier transform of $\mu\text{SR}$ data (triangles) and fit (solid line) in Fig. ?? and of the best fit to Eqs. 3.1.4 and 4.2.1 without alternating fields (dashed line). (b) The high-field in greater detail. Notice the improved fit in the high field tail due to the alternating fields, corresponding to the vortex core area. . . . .	58
5.7	Amplitude of vortex core alternating magnetic fields measured by $\mu\text{SR}$ vs. temperature, for applied fields of $\mu_0 H = 1$ T (nablas) and $\mu_0 H = 4$ T (full squares). . . . .	59
5.8	Neutron counts near $q_{AF}$ for $L = 0$ , in zero field (closed squares) and in a field of $\mu_0 H = 2.6$ T (closed triangles). The peak near $H = -0.48$ r.l.u. is a signal from an impurity phase in the crystal. . . . .	60
5.9	Neutron counts near $q_{AF}$ for $L = 2$ , in zero field (closed squares) and in a field of $\mu_0 H = 2.6$ T (closed triangles). The peak near $H = -0.44$ r.l.u. is a signal from an impurity phase in the crystal. . . . .	62
5.10	Neutron counts near $q_{AF}$ for $L = 4$ , in zero field (closed squares) and in a field of $\mu_0 H = 2.6$ T (closed triangles). . . . .	63

- 5.11 Panel (a): Temperature dependence of the magnetization in a small field as the sample is cooled through  $T_c = 13.8$  K Panel (b): Main internal magnetic field (left) and the late-time  $\mu$ SR signal amplitude as the temperature is decreased through  $T_N$ . The low temperature value of the signal indicates that the *entire* sample undergoes the transition to AF (right). The data indicate that within experimental resolution  $T_N = T_c$ . See text for details of the curve. The curve through the internal magnetic fields (left) is a fit to  $B_{AF} = B_0 * (1 - T/T_N)^\beta$ , where  $\beta = 0.22(2)$  and  $B_0 = 273(7)$  G. . . . . 65
- 5.12 Early time  $\mu$ SR polarization signal in ZF at  $T = 3$  K (closed  $\square$ ) and at  $T = 50$  K ( $\triangle$ ). The low temperature data show an oscillation corresponding to an average field of 273 G at the muon site. The rapid damping of the oscillations is caused by the presence of another magnetically inequivalent muon site and a broad distribution of fields at the sites. The curve through the data is a three component fit: a fast and slow exponential and a damped cosine. The high temperature signal is characteristic of a phase with no internal electronic fields. The curve through the high temperature data is a gaussian, whose small damping constant is caused by nuclear dipoles. . . . . 66
- 5.13 Muon polarization signal (multiplied by asymmetry) in  $YBa_2Cu_3O_{6.35}$  at  $T = 4$ K in zero field, taken with 20 million events. The curve is a fit to three gaussian damped frequencies and an additional slow relaxing exponential function. The kink in the data near  $t = 0.1\mu s$  reveals an additional high frequency near 9 MHz, which is binned over in fig. 5.12. 68
- 5.14 Late-time muon polarization signal at  $T > T_N$  ( $\triangle$ ) and at  $T < T_N$  (closed  $\square$ ). As the temperature is lowered through  $T_N$ , the late-time  $\mu$ SR signal decreases as the large internal magnetic field depolarize the signal rapidly. . . . . 70

# Acknowledgements

I would like to thank Heydar Radjavi, my supervisor, for his many suggestions and constant support during this research. I am also thankful to Matjaž Omladič for his guidance through the early years of chaos and confusion.

Professor Y.A. Abramovich expressed his interest in my work and supplied me with the preprints of some of his recent joint work with C.D. Aliprantis and O. Burkinshaw, which gave me a better perspective on my own results. Heinz Bauschke shared with me his knowledge of convex analysis and provided many useful references and friendly encouragement.

I had the pleasure of meeting the Killam trustees. They are wonderful people and their support makes research like this possible. The *Izaak Walton Killam Memorial Scholarship*, which was awarded to me for the period 1991–1994, was crucial to the successful completion of this project.

I should also mention that my graduate studies in Canada were supported in part by the Research Council of Slovenia.

Of course, I am grateful to my parents for their patience and *love*. Without them this work would never have come into existence (literally).

Finally, I wish to thank the following: Francisco (for his friendship); Adriana (for changing my life from worse to bad); Maks and Lili (for the painful introduction to the art of paragliding); Karen, Kelly, Linda, Rick, Maja, Paul, Phil, Michelle, Peter, Wendy, Scott, Eve, George, Andrew, Rob ... (for all the good and bad times we had together); Stephen and Bill (for special effects); Ludwig van Beethoven and The Rolling Stones (and they know why); *and* my brother (because he asked me to).

Halifax, Nova Scotia  
December 7, 1994

Aleksander Simonič

# Chapter 1

## Introduction

Superconductors are characterized by a low temperature state with zero resistivity to current flow, and partial flux expulsion at the edge of a superconductor (Meissner state) or in the bulk (vortex state), in the presence of an applied field. These characteristics are due to the formation of a superconducting state at low temperatures where fermionic electrons form bosonic pairs that condense into a lower energy state. The establishment of an energy gap in momentum space ( $\Delta_{\vec{k}}$ ), between the lowest energy state and excited states, exists in all superconductors at zero field and temperature on at least part of the Fermi surface. High temperature superconductors exhibit a non-zero gap at four nodes of the Fermi surface, due to a *d*-wave ( $\Delta_{\vec{k}} \propto (k_x^2 - k_y^2)$ ) nature of their order parameter, while conventional superconductors are fully gapped at all points of the Fermi surface ( $\Delta(\vec{k}) = \Delta_0$ ).

The application of a large external magnetic field ( $H_a$ ) distinguishes two types of superconductors: type-I superconductors fully expel the applied field in the bulk, while in type-II superconductors the applied field penetrates the superconductor in the form of a vortex lattice, tubes of magnetic flux generally ordered in a regular lattice (at low temperatures  $T \ll T_c$  and at low external magnetic fields). High

temperature superconductors fall into the type-II class of superconductors, like a number of conventional superconductors such as  $\text{NbSe}_2$ ,  $\text{Nb}_3\text{Sn}$ ,  $\text{V}_3\text{Si}$ , etc.

A second characteristic that distinguishes high temperature superconductors from conventional ones is a phase diagram that many high- $T_c$ 's share in common. The depletion or addition of a chemical component, known as charge doping, changes the behaviour of the material from that of a Mott insulator[35, 55] to a superconductor at optimal doping, defined as the doping that exhibits the highest critical temperature. Thus, a prevailing consensus is that the underdoped superconductor, where the density of charge carriers is low, should be viewed as a doped Mott insulator.

This region in between the insulating phase and optimal doping, referred to here as underdoped, is poorly understood. Perhaps more poorly understood is the normal phase of underdoped superconductors. Numerous experiments have suggested the presence of “pseudogap” above  $T_c$  which persists to room temperature in the underdoped cuprates and has the same  $d$ -wave symmetry as the superconducting gap. The pseudogap does not fully gap excitations probed by optical spectroscopy, hence the name “pseudo”. The presence of a gap, however, suggests the formation of pairs in a lower energy state at  $T^*$ , that condense into a superconducting ground state at  $T_c$ .

The ground state physics of this unusual state is difficult to probe because in the cuprates  $T_c$  is of the order of 100 K. Hence probing the state at low energies requires creating a normal state at low temperature. This state can be achieved, as was pointed out by Franz and Tesanović[33], by applying an external magnetic field and creating a vortex lattice. The physics of the vortex cores in the underdoped cuprates is likely to reflect the low temperature ground state of the “pseudogap” state. Secondly, heavily underdoped cuprates can be investigated, where  $T_c$  is near zero.

Pure crystals are very difficult to grow in this area of the phase diagram, however, and little progress has been achieved here.

In this thesis, I present measurements in the vortex state of underdoped  $\text{YBa}_2\text{Cu}_3\text{O}_{6.50}$  and in zero field of heavily underdoped  $\text{YBa}_2\text{Cu}_3\text{O}_{6.35}$ . These results suggest that the vortex cores of underdoped  $\text{YBa}_2\text{Cu}_3\text{O}_{6+x}$  may be antiferromagnetic, reflecting the proximity in the phase diagram to the antiferromagnetic parent compound, and that the ground state of heavily underdoped  $\text{YBa}_2\text{Cu}_3\text{O}_{6+x}$  is likely a bulk state where superconductivity and disordered antiferromagnetism coexist.

Chapter 2 reviews experimental results in the  $\text{YBa}_2\text{Cu}_3\text{O}_{6+x}$  family relevant to this thesis. The theory of type-II vortex lattice field distribution is reviewed in chapter 3. Two classes of theories predicting anomalous magnetism in the vortex state of the cuprates are also described. Chapter 4 explains the three experimental methods used in this thesis: SQUID magnetization,  $\mu^+$ SR, and neutron scattering. Results are presented on  $\text{YBa}_2\text{Cu}_3\text{O}_{6.35}$  and  $\text{YBa}_2\text{Cu}_3\text{O}_{6.50}$  in chapter 5. Finally, Chapter 6 proposes models for the results in  $\text{YBa}_2\text{Cu}_3\text{O}_{6.35}$  and a reconciliation of the results from neutron scattering and  $\mu^+$ SR in  $\text{YBa}_2\text{Cu}_3\text{O}_{6.50}$ .

# Chapter 2

## $\text{YBa}_2\text{Cu}_3\text{O}_{6+x}$

The  $\text{YBa}_2\text{Cu}_3\text{O}_{6+x}$  family of superconductors was discovered[?] less than a year after Berdnoz and Muller's discovery of high temperature superconductivity in the  $\text{La}_{2-x}\text{Sr}_x\text{Cu}_2\text{O}_4$  compounds[?]. With an optimal  $T_c$  near 93K, this family of superconductors is probably the most studied of the high- $T_c$  families discovered so far. In this chapter, I will review the chemical structure of  $\text{YBa}_2\text{Cu}_3\text{O}_{6+x}$ , and outline general properties of the system as a function of doping. Then, experimental evidence for magnetic behaviour both in zero field and in an applied field will be reviewed. While relevant experiments on other high- $T_c$  compounds will also be mentioned, references are restricted to those relevant to this thesis' results.

### 2.1 Chemical Structure of $\text{YBa}_2\text{Cu}_3\text{O}_{6+x}$

Figure 2.1 shows the chemical structure of the  $\text{YBa}_2\text{Cu}_3\text{O}_{6+x}$  compound. At the centre of the unit cell, the yttrium atom (valence  $\text{Y}^{3+}$ , all valences below for  $\text{YBa}_2\text{Cu}_3\text{O}_{6.60}$ ) is sandwiched by two layers of  $\text{CuO}_2$  planes, where the copper adopts a  $\text{Cu}^{+2}$  valence. The barium atom (valence  $\text{Ba}^{2+}$ ) separates the  $\text{CuO}_2$  planes from layers of another  $\text{CuO}$  structure, known as the chains. In the chains, the copper is  $\text{Cu}^{+1}$ . Two planes

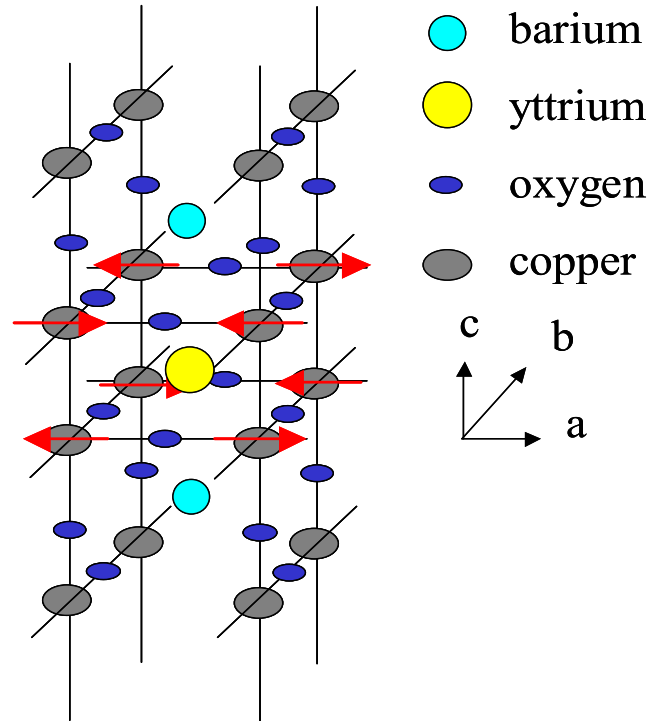


Figure 2.1: Structure of  $YBa_2Cu_3O_{6+x}$ . The  $Cu^{2+}$  spins in the Cu-O planes are shown with red arrows. The chains here are shown with oxygen between the Cu chain ions. Both the superconductivity and antiferromagnetism occur in the Cu-O planes.

in units cells stacked along the  $c$ -axis are separated by  $11.67\text{\AA}$  in the optimally doped sample, while the Cu-O bond in the planes is  $3.83\text{\AA}$  along the  $a$ -axis and  $3.87\text{\AA}$  along the  $b$ -axis.

Generally, one may regard the  $YBa_2Cu_3O_{6+x}$  system as hole-doped planes weakly coupled with the chains and the barium and yttrium ions acting as charge reservoirs. The interaction of the chains, where superconductivity has also been reported [REF], with the planes, complicates the problem of determining the physical interactions that govern the electronic behaviour of the system, unlike in single-plane  $La_{2x}Sr_xCu_2O_4$  or

$T_h??Cu_2O_4$ . On the other hand, the availability of double, or triple-plane systems such as *BSSCO* and  $Bi_2Sr_2CaCu_2O_8$  has allowed researchers to study the interplay of the chains and planes in the high- $T_c$ 's. The added complication of the chains is partly redeemed by the availability of arguably the cleanest samples, and the possibility of growing large single crystal in the underdoped region of the phase diagram.

## 2.2 Evolution of behaviour with doping

Soon after the 1986 discovery of high temperature superconductivity,  $\mu^+$ SR[40, 41] and neutron scattering [?] established that the parent compound,  $YBa_2Cu_3O_{6+x}$  is a well ordered insulating antiferromagnet with a Neel temperature  $T_N > 500K$ . The  $Cu^{2+}$  spins order antiferromagnetically in the Cu-O planes, and the planes are coupled antiferromagnetically. In later experiments,  $\mu^+$ SR detected at least two frequencies[7, 8], indicating either multiple muon site, inhomogeneous magnetism, or varying moment magnitude. Neutron studies showed that the ordered moment lies in the  $a - b$  plane and is approximately 0.65 of a Bohr magneton in magnitude[?].

Theoretical models for the cuprates are numerous. Often the starting point is the physics of the Mott-insulator parent compound. It is often described by the Hubbard one band model[10], where the atomic sites are assume to be half filled. The large Coulomb on-site repulsion energy ( $U$ ) is greater than the hopping energy ( $t$ ), which leads to a lower energy for antiferromagnetically coupled neighbouring spins than for ferromagnetically coupled spins. However, the effect of introducing holes in the model, and how they lead to superconductivity, is poorly understood.

Annealing samples in higher oxygen partial pressure increases  $x$  and destroys the

antiferromagnetic state rapidly. Additional oxygen are thought to migrate preferentially to the O1 position shown in Fig.2.1, creating chains along the  $b$ -axis and furnishing hole-like mobile charge carriers. At a poorly established oxygen concentration, near  $x = 0.35$  and  $n_h = 0.1$ , superconductivity appears. The increasing hole concentration on the chains is thought to migrate to the planes once the Cu-O chains attain a sufficient length, likely three or four neighbouring oxygen atoms along the  $b$ -axis. These holes then form the mobile carriers that condense into pairs. The nature of this condensation and the attractive mechanism is still unknown.

The transport and magnetic properties of this underdoped region, where  $T_c \ll T_c^{max}$  and  $T_N \ll T_N^{max}$ , are still poorly understood. One outstanding question is the hole dependence of the  $T_N$  and  $T_c$  curves in this heavily underdoped region. Three possibilities are shown in fig. 2.2. Do the two curves intersect at a critical doping, as in Fig. 2.2(a), with coexisting superconductivity and antiferromagnetism over a finite range of hole doping; do they not meet as in Fig. 2.2(b) and if so what is the physics in between the two curves at low temperature; or do the two curves cross over at finite temperature, indicating that superconductivity and magnetism coexist microscopically, as in Fig. 2.2(c)? Furthermore, in this doping regime, the magnetism is clearly not long-range, the Neel temperature is greatly reduced. The nature of the magnetism is also unclear. These questions are addressed by my study of  $YBa_2Cu_3O_{6.35}$  in chapter ??.

As the oxygen content is further increased,  $T_c$  rises rapidly to a 60K plateau, over the range  $x = 0.50$  to  $0.8$  and then increases again to another plateau near optimal doping  $x = 0.95$ , with  $T_c^{max} = 93K$ . For  $x > 0.5$ , no evidence of large ordered and homogeneously distributed magnetic moments have been found either in zero or a finite

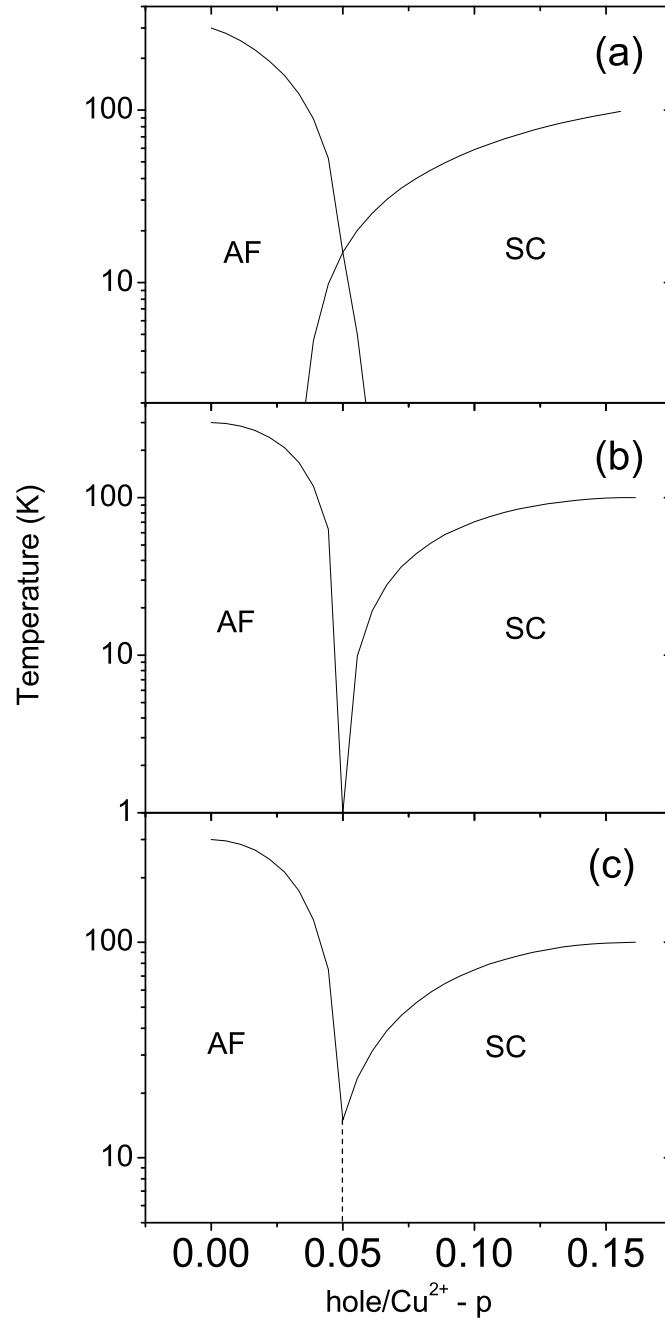


Figure 2.2: Possible phase diagrams near the AF/SC boundary ( $p = 0.05$ ) in clean, homogeneous crystals. Panel (a): coexistent SC and AF over a range of hole doping, possibly indicating competition between the two; panel (b) no coexistence between AF and SC at non-zero temperatures; panel (c) a transition at non-zero temperature to a state characterized by coexistent AF and SC.

applied field. Superconductivity is instead robust to high temperatures, and below  $x^{max}$  a second higher temperature scale has been detected with angular resolved photon emission spectroscopy (ARPES)[?], scanning tunneling microscopy (STM) [?], and microwave spectroscopy [?]. This “pseudogap” is formed at temperatures well in excess of  $T_c$  and has also been detected in the vortex cores of  $Bi_2Sr_2CaCu_2O_8$ [?].

The magnetic and superconducting behaviour of the cuprates at the undoped and optimally doped ends of the phase diagram, respectively, suggest that the two states are competitive and cannot coexist. This is generally true when magnetic ions are substituted into conventional superconductors. However, evidence quickly accumulated that coexistence at low temperatures of these two states may actually be possible, either in zero magnetic field, or in the presence of a magnetic field. Here, some evidence for such behaviour is reviewed.

## 2.3 Magnetic behaviour in Zero Field

The superconducting state exhibits a Meissner state in small magnetic fields, where the applied magnetic field is screened from the bulk by circulating currents. In conventional superconductors, the Meissner state is characterized by an isotropic  $s$ -wave gap and no states at the Fermi energy. In contrast, the cuprates have nodes in the gap and therefore low energy excitations at finite temperature. Furthermore, the proximity to the undoped insulating state may lead to magnetic behaviour in zero field in the Meissner state.

### 2.3.1 $\mu^+$ SR measurements

$\mu^+$ SR and neutron scattering have provided much information on magnetism in zero field. Zero field experiments by Nishida *et al.*[40, 41], Kiefl *et al.*[25], Brewer *et al.*[7, 9, 8], and Niedermayer[39] (for Ca-doped  $YBa_2Cu_3O_{6+x}$ ) have mapped out the phase diagram in powdered samples. The “4 MHz” muon site identified by Nishida *et al.* corresponds to muons sampling a site in the crystal lattice where the magnetic field is approximately 300 G. Brewer *et al.* identified another “18 MHz” site (corresponding to 1330 G at this muon site). Kiefl *et al.* showed that this signal is present to  $T = 20$  mK. Kiefl *et al.*[25] and Brewer *et al.*[8] presented a phase diagram for  $YBa_2Cu_3O_{6+x}$  with a sharply decreasing  $T_N$  for  $x < 0.4$  where the field at the “4 MHz” muon site remains constant. At higher doping ( $x \geq 0.4$ ), the magnetic field at the site decreases rapidly and the field distribution at the muon site grows. Samples begin to show evidence of superconductivity with  $T_c$ 's reaching 60K above  $x \geq 0.5$ . Some samples with  $0.38 \leq x \leq 0.50$  were both magnetic and superconducting at low temperatures.

Niedermayer *et al.*[39] established the phase diagram for Ca doped  $YBa_2Cu_3O_{6+x}$  in greater detail. At low doping, holes are difficult to dope into the planes; the introduction of  $Ca^{2+}$  for  $Y^{3+}$  allows researchers to control the hole concentration at low doping, but may alter some properties of the superconductor due to the distortions that the Ca introduces[?]. Generally, they found a similar phase diagram to Brewer *et al.* and Kiefl *et al.*; however, their samples exhibited superconductivity at slightly higher hole concentration,  $n_h > 0.50$ . Furthermore, they identified two different doping regimes at low hole concentration. The lower one ( $n_h < 0.04$ ) showed the rapidly decreasing Neel temperature and constant magnetic field at the muon site. Above

$n_h > 0.2$ , they found a slowly decreasing magnetic transition temperature they labelled a glass transition, with a sharp increase in the field distribution width at the muon site and a corresponding decrease in the average field. This state persisted into the third, superconducting phase.

### 2.3.2 Neutron Measurements

The underdoped regime has also been examined by P. Dai *et al.*[13] with polarized and unpolarized neutrons. They find evidence for a spin gap, incommensurate low energy spin fluctuations, and a sharp commensurate resonant feature at higher energy. As will be discussed in Chapter ??, neutrons can measure a magnetic signal at reciprocal lattice vectors,  $q_AF = (1/2, 1/2, L)$ , where  $q$  is defined in terms of the Cu-O planar unit cell. Incommensurate scattering, where  $q_AF = (1/2 - \delta, 1/2 - \delta, L)$ , for instance, signifies that the magnetism is incommensurate with the unit cell. Tranquada first interpreted such scattering in  $La_{2-x}Sr_xCu_2O_4$  in terms of stripes with a magnetic unit cell length in the Cu-O planes of  $1/\delta$ [51].

Dai *et al.* find that a spin gap in the magnetic fluctuations spectrum develops at low energies that is proportional to  $T_c$ . Above this gap, low energy fluctuations with an incommensurate wavevector appear above  $T_c$  and  $\delta$  increases with  $T_c$ , saturating at  $\delta = 0.1$  for  $x > 0.6$ . This low energy spectrum gives way to the resonance found at  $E = 40$  meV in optimally doped  $YBa_2Cu_3O_{6+x}$ , where it appears at  $T_c$ . In underdoped  $YBa_2Cu_3O_{6+x}$ , the resonance appears well above  $T_c$ .

Figure 2.3 shows measurements of  $T_N$  and  $T_c$  made by neutron and  $\mu^+$ SR in  $YBa_2Cu_3O_{6+x}$ . We note that in agreement with the scenarios in fig. 2.2, sharp decreases in  $T_N$  and  $T_c$  occur near  $x = 0.35$ , which corresponds to  $n_h \approx 0.3$  0.4.

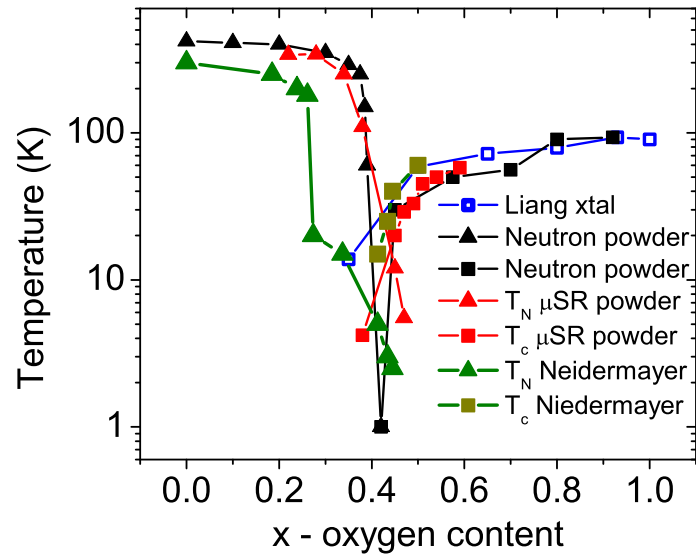


Figure 2.3:  $T_N$ 's and  $T_c$ 's taken from various  $\mu^+$ SR and neutron experiments in  $YBa_2Cu_3O_{6+x}$ . Notice that all experimental data agrees with a large decrease in  $T_N$  and  $T_c$  near  $x = 0.3 - 0.4$ .

Each scenario is also consistent with some of the data.

## 2.4 Magnetic behaviour in an applied field

The application of a magnetic field greater than  $H_{c1}$  creates the vortex state in the cuprates, which persists to an upper critical field  $H_{c2}$ .  $H_{c1}$  and  $H_{c2}$  are estimated to be approximately 100-200 G and 100 T in optimally doped  $YBa_2Cu_3O_{6+x}$ . The applied field in the bulk is quantized in vortices of flux  $\Phi_0$ , whose radius is approximately given by the coherence length ( $\xi$ ). The magnetic field decreases away from the vortex core to a minimum, over the length scale of the penetration depth ( $\lambda$ ). The cores of the vortices in conventional superconductors resemble “normal” state matter; both theory (see Chapter 3) and experiment suggest that this may not be so in the cuprates. Below numerous experiments suggesting anomalous magnetic properties in the vortex state are reviewed. Scanning tunnelling measurements (STM) have also suggested that the pseudogap state, found at high temperatures in many underdoped cuprates, may also exist in the vortex cores of  $Bi_2Sr_2CaCu_2O_8$ [43].

Furthermore, the vortex lattice that is formed by these flux lines can behave as a classical or quantum mechanical object. Phase transitions as a function of disorder (induced by crystal defects), temperature, and magnetic field have been measured. Sonier *et al.* have also shown that an increasing magnetic field seems to decrease the vortex core radius measured by  $\mu^+$ SR while increasing the effective penetration depth[23]. Some experimental results relevant to this thesis’ results are reviewed below.

### 2.4.1 Magnetism induced by the Vortex State

Recently a number of experiments have indicated that the application of a magnetic field may be able to induce or amplify magnetism in the vortex state. Vaknin *et al.*[11] reported that the application of a 5 Tesla field induces additional broad scattering centered at the antiferromagnetic wavevector,  $q_{AF}$ . From the width in reciprocal space of the signal, they concluded that it could originate from the vortex cores. The sample was a twinned single crystal (50 mg) grown in an yttria-stabilized zirconia crucibles with a  $T_c = 90$  K.

Lake *et al.*[27] used inelastic neutron scattering (see Chapter ??) to measure scattering near  $q_{AF}$  in optimally doped  $La_{2x}Sr_xCu_2O_4$  with and without a 7.5 Tesla magnetic field. They found enhanced scattering in the presence of the field below the zero field spin gap. The application of a small field (relative to  $H_{c2}$ ) recovers all the intensity measured at  $E = 2.5$  meV in the normal state. Furthermore, the magnetic correlation length of the incommensurate scattering in a field at low temperature is greater than 20 times the Cu-O plane length scale (3.77Å in  $La_{2x}Sr_xCu_2O_4$ ). They conclude that the vortex cores are small dynamic antiferromagnets due to the small size of the cores. Various magnetic correlation lengthscales of the spins point to anisotropic correlations between the cores.

Nuclear magnetic resonance has also contributed to our understanding of magnetism in the vortex core. Mitrovic *et al.*[?] have measured magnetic fluctuations in planar  $^{17}O$  in optimally doped  $YBa_2Cu_3O_{6+x}$  in applied fields up to 37 Tesla. They scan the frequency of the applied radiation through the field distribution of a superconductor in the applied field. At low temperature and high fields, they find an increase in  $1/TT_1$  at frequencies associated with the vortex core, which they attribute

to either bound states in the cores at non-zero energies or antiferromagnetism in the cores.

Finally, Dai *et al.*[12] measured the field dependence of the large neutron resonance in  $YBa_2Cu_3O_{6+x}$ [66]. They found that a  $H = 6.7$  T field reduces the resonance amplitude by 30% and 10%, for a field along the  $c$ -axis and in the  $a - b$  plane, respectively. For this doping, the resonance is present well above  $T_c$ , but the change with magnetic field seems to occur near  $T_c$ .

## 2.4.2 Evolution of the Vortex Lattice with Temperature and Magnetic Field

As will be discussed in Chapter 3, the influence of temperature and disorder profoundly modifies the vortex lattice. Thermal fluctuations, large in the high- $T_c$ 's, melt the vortex lattice to a vortex liquid state, at temperatures well below the  $T_c$ . Furthermore, disorder leads to a cross over to a glassy phase with unknown spatial order, and perhaps a low temperature reentrant liquid phase, just above  $H_{c1}$ . As expected, numerous experiments have reported a melting of the vortex lattice and a cross-over with increasing magnetic field in optimally or near-optimally doped  $YBa_2Cu_3O_{6+x}$ [42, 44, 14, 52, 6, 46], underdoped  $YBa_2Cu_3O_{6+x}$ [48, 18] and  $Bi_2Sr_2CaCu_2O_8$ [56, ?].

### Thermal Fluctuations and Melting of the Vortex Lattice

Liang *et al.* [42] measured a first-order melting transition in optimally doped  $YBa_2Cu_3O_{6+x}$  ( $T_c = 93.1$ K), using a commercial SQUID with second derivative pick

up coils. The solid phase has lower flux density, indicated by an increase in the magnetisation in the liquid state compared to the low temperature solid state. The small number of pinning sites in the clean sample was credited with moving the irreversibility line to lower temperatures than the melting line. They also noted that a similar first order transition was not found in Ni-doped samples or twinned samples. Welp *et al.* [52] report similar magnetization measurements in an optimally doped sample of  $YBa_2Cu_3O_{6+x}$  ( $T_c = 92.7K$ ). They also show that the resistivity drops to zero at this melting transition, indicating that the magnetisation jump does coincide with a transition to a low temperature non-dissipative pinned vortex lattice. Their measurements of  $H_{melt}(T)$  indicate that the melting line remains at fairly high temperature, with  $H_{melt}(T = 81.5K) = 5.7T$ .

Another means of probing the vortex lattice transition is by measuring another thermodynamic variable, the specific heat. By measuring  $\Delta C(T, B) = C(T, B) - C(T, B = 0)$ , Roulin *et al.* find a small peak in  $\Delta C(T, B)$  in two slightly underdoped  $YBa_2Cu_3O_{6+x}$  crystals ( $x = 6.94, 6.96$ , BaZrO<sub>3</sub> crucible-grown, quenched in oxygen and twinned) and one overdoped crystal ( $x = 7.00$ , as above, slow anneal). In the most underdoped sample, they find that below  $H = 3T$  a step in  $\Delta C(T, B)$  indicates a second order transition; that between  $B_{tcr}^{low} = 3T < B < 9.5 = B_{tcr}^{high}T$  the transition is first order (corresponding to a peak in  $\Delta C(T, B)$ ); and above  $9.5T$  the transition is again second order up to  $B_{cr} = 11.5T$ , defining a critical point. In the other underdoped and the overdoped samples, the first-order transition persists up at least  $B_{tcr}^{high} = 16T$ , while  $B_{tcr}^{low}$  increases to  $6T$ , indicating that slight changes in oxygen stoichiometry have large effects on the vortex lattice phase diagram near optimal doping. Finally, they compare  $YBa_2Cu_3O_{6+x}$  crystals of identical doping ( $x = 0.95$ )

grown by the travelling solvent floating zone method (TSFZM) with  $BaZrO_3$  crucible grown crystals. The melting line moves to lower temperatures in the TSFZM crystals, and only second-order transitions are visible, indicating a glassy low temperature phase. TSFZM crystals typically have a larger density of pinning site, are less well ordered, and contain a  $YBa_2Cu_3O_5$  phase.

In heavily underdoped samples ( $x < 0.8$ ), the melting line shifts to lower temperatures significantly.  $\mu^+$ SR measurements[46] in  $YBa_2Cu_3O_{6.60}$  (crucible grown, twinned and untwinned,  $T_c = 59K$ ) show a drop-off in  $1/\lambda_{ab,eff}^2$  near a magnetic field dependent melting temperature, correlated with a drop in the skewness of the magnetic field distribution. Due to the field dependence of  $T_m$ , Sonier *et al.* attribute the transition to a decoupling of layers in a liquid state, eg. a  $3D - 2D$  transition in a liquid.

question: how can the transition be from liquid to liquid, if you see long range order in the muSR lineshape?

question: large floating zone xtals show only 2nd order transition, meaning low T phase is a "glass". SANS shows 2nd order case, eg. no long range order? CM. Aegerter private comm. check for CM Aegerter papers around 1998 in YBCO SANS

### **Disorder induced crossover with field**

In optimally doped  $YBa_2Cu_3O_{6+x}$ , Bouquet *et al.*[6] report a crossover to a glassy phase at low temperature in a field of 10T near the melting line  $T \approx 75K$ . Using a torque magnetometer, they measure a broad second peak in the magnetization as a function of magnetic field, below  $T_{irr}$ , the so-called "fishtail". This feature is taken as a signal of the glassy phase crossover from an ordered lattice. Their measurements are

in the temperature range  $60K < T < 75K$ , and show a linearly increasing crossover with increasing temperature. They note that the low temperature measurements  $T \geq 60K$  have a large uncertainty associated with them. At higher field still, the vortex glass phase gives way to a vortex liquid.

Ling *et al.*[?] report a peak effect in AC susceptibility measurements on a crystal of  $YBa_2Cu_3O_{6.55}$  crystal ( $T_c = 56.0K$ ). Associating the peak effect with the vortex lattice(Bragg Glass)/liquid melting transition indicates that the melting line in this crystal has also moved to lower temperature:  $H_m(T = 47K) \approx 0.5T$ , with a linear relation between  $H_m$  and  $T$  (within uncertainties). Abrego *et al.* have made similar AC susceptibility measurements in an underdoped  $YBa_2Cu_3O_{6+x}$  crystal ( $T_c = 62.8K$ , quenched) as a  $3D - 2D$  crossover at  $H = 0.9T$  near  $T = 47K$ .

I note an important neutron measurement by Klein *et al.*[24] of the field dependence of a Bragg peak in the superconductor  $(K_a, Ba)BiO_3$  ( $T_c = 23K$ ). Klein *et al.* demonstrated the “glassy” nature of the vortex phase in low fields in this three dimensional material, up to magnetic fields of  $H = 0.7T$ . Below this magnetic field, the Bragg peak is visible; it disappears rapidly above this crossover field *without* broadening. This is a direct prediction of Giamarchi and Doussal’s Bragg glass theory[15] and indicates that long range order exists in the low field Bragg glass phase and disappears in the high field vortex glass phase. The width of the Bragg peak corresponds to a longitudinal collective pinning length,  $L_c = 90\text{\AA}$ (defined by  $u \approx \xi$  when  $L = L_c$ , where  $L$  is the length of the vortex line)[?]. They show that the crossover field agrees with the location of the peak effect measured by ac susceptibility, indicating that the peak effect is related to a change in the vortex lattice structure.

Finally, Sonier *et al.*[46] attribute a low-field tail in the Fast Fourier transform

of the  $\mu^+$ SR polarization signal in  $YBa_2Cu_3O_{6.60}$  (twinned) to a  $2D$  vortex lattice, at  $H = 2.9T$  and low temperature. However, this signal was not seen in a similar detwinned signal.

In conclusion, transport,  $\mu^+$ SR, magnetisation, Hall probe and specific heat measurement have provided evidence for a novel vortex state phase diagram in  $YBa_2Cu_3O_{6+x}$ . In clean samples, the low temperature, low field state is likely a vortex lattice with good long range order, which melts with increasing temperature to a vortex liquid. At higher field, a crossover to a vortex glass appears, around  $H = 10T$  and  $T = 70K$  in optimally doped  $YBa_2Cu_3O_{6+x}$ , followed by further transitions to liquid states at higher fields. The low temperature behaviour of this crossover line is unclear from magnetization and specific heat measurements, although theoretical considerations and the neutron measurements of Klein *et al.* and Jourdain *et al.* would lead to a *decrease* in field with decreasing temperature.

Dirtier samples can also show evidence for a vortex liquid reentrant state at very low fields, close to  $H_{c1}$  and at low temperatures and the ordered lattice phase is replaced by a vortex glass. Underdoping can greatly alter the melting and lattice/glass transitions, by shrinking the area of the ordered lattice phase, although sample purity, and the effects of twinning also have as great a role in determining the phase diagram.

# Chapter 3

## Theory

As seen in the previous section, the application of a magnetic field to high- $T_c$  superconductors drives them into a “vortex state”, characterized by partial penetration of the magnetic field in a lattice of vortices. The first part of this chapter is devoted to a brief discussion of models of the magnetic field distribution in a superconductor and the effects of thermal fluctuations and disorder on the vortex lattice. The second part examines various theories that predict the appearance of anomalous magnetism in the vortex and Meissner state of superconductors.

### 3.1 Superconductors and the Vortex State

Abrikosov first provided a solution to the magnetic field profile in a type-II superconductor, when the applied field exceeds the lower critical field,  $H_{c1}$ . The magnetic field penetrates the superconductor in the form of tubes of magnetic flux, arranged on a hexagonal lattice. The hexagonal configuration represents the lowest energy state of the vortex lattice, but a square lattice can also occur when nonlocal and nonlinear

effects in the magnetic field distribution are taken into account[20].

### 3.1.1 The London Model

A simple periodic solution to the problem of a superconductor in an external magnetic field ( $\mu_0 H$ ) is given by the London Model[50]. The London Equation, in the low field limit where the superconducting order parameter is constant in space and the magnetic field is applied along the  $z$ -axis, is given by:

$$\vec{B}(\vec{r}) + \vec{\nabla} \times (\vec{\nabla} \times \vec{B}(\vec{r})) = \Phi_0 \sum_{\nu} \delta(\vec{r} - \vec{r}_{\nu}) \quad (3.1.1)$$

A periodic solution is assumed for  $\vec{B}(\vec{r})$ :

$$\vec{B}(\vec{G}) = \int \vec{B}(\vec{r}) e^{-i\vec{G}\cdot\vec{r}} d^2\vec{r} / S \quad (3.1.2)$$

Substituting Eq.3.1.2 into Eq.3.1.1:

$$B(r) = \frac{\Phi_0}{S} \sum_G e^{-i\vec{G}\cdot\vec{r}} \frac{F(u)}{1 + \lambda_{ab}^2 G^2} \quad (3.1.3)$$

where  $u^2 = \xi_{ab}^2 G^2$ ,  $\vec{G}$  is a reciprocal lattice vector of the vortex lattice,  $b = H/H_{c2}$  is the reduced field,  $H_{c2}$  is the upper critical field,  $\Phi_0$  is the flux quantum, and  $S$  is the area of the reduced unit cell for a hexagonal lattice.

For the London solution,  $F(u) = 1$ . The London solution diverges inside the vortex core ( $r < \xi_{ab}$ ) and therefore the sum in Eq. 3.1.3 stops at  $G_{max} = 1/\xi_{ab}$  and a cut-off function ( $F(u)$ ) is introduced. Usually it is taken to be  $F(u) = e^{-u^2/2}$ .

The London solution is valid at all temperatures, but only at moderately low magnetic fields,  $H_{c1} < H \ll H_{c2}$ , where the magnetic field does not change the value of the superconducting order parameter  $\Psi(r) = \Psi_0$ .

### 3.1.2 The Ginzburg-Landau Model

Another approach is to use a variational solution to the Ginzburg-Landau free energy expansion. Yaouanc *et al.*[1] showed that the vortex core's effect on the field distribution could be better modelled by replacing the Gaussian cutoff in Eq.3.1.3 with a Bessel function, eg:

$$\vec{B}(\vec{r}) = \frac{\Phi_0}{S}(1 - b^4) \sum_G e^{-i\vec{G}\cdot\vec{r}} \frac{uK_1(u)}{1 + \lambda_{ab}^2 G^2} \quad (3.1.4)$$

where  $u^2 = 2\xi_{ab}^2 G^2(1 + b^4)[1 - 2b(1 - b)^2]$  and  $K_1(u)$  is a modified Bessel function. This model, however, is strictly valid only near  $T_c$ , and at lower magnetic fields ( $b \ll 1$ ).

### 3.1.3 Non-local Effects, Microscopic Models, and *d*-wave symmetry

The London and GL-equations above are local equations, meaning that the magnetic field vector potential  $\vec{A}(\vec{r})$  depends on the current distribution  $\vec{j}(\vec{r})$  only at  $\vec{r}$ . At higher magnetic fields, the non-local relation between  $\vec{A}$  and  $\vec{j}$  becomes more important [?]. A linear approximation in Fourier space gives  $\vec{A}(\vec{k}) = \hat{Q}(\vec{k})\vec{j}(\vec{r})$ . These non-local corrections can be introduced either as higher order corrections to a free energy[20], the derivation of modified London equations from the quasiclassical Eilenberger equations[26] or more correctly by the introduction of a  $\hat{Q}(\vec{k})$  in Eq.3.1.3[20, 36, 37]:

$$B(\vec{r}) = \frac{\Phi_0}{S} \sum_G e^{-i\vec{G}\cdot\vec{r}} \frac{F(u)}{1 + G_i G_j Q_{ij}(\vec{G})/\det(\hat{Q})}, \quad (3.1.5)$$

where

$$Q_{ij}(\vec{G}) = \frac{4\pi}{\lambda_{ab}^2} \sum_{n>0} \left\langle \frac{\Delta_{\hat{p}}^2 \hat{v}_{Fi} \cdot \hat{v}_{Fj}}{\sqrt{\Delta_{\hat{p}}^2 + \omega_n^2} (\Delta_{\hat{p}}^2 + \omega_n^2 + \gamma_{\vec{G}}^2)} \right\rangle \quad (3.1.6)$$

Amin *et al.* have shown that these effects account quantitatively for the magnetic field dependence of the second moment of the field distribution measured by  $\mu^+$ SR[47, 37]. Hence, the measured field dependence of  $\lambda_{ab}$  is attributed to these nonlocal effects.

Although the  $d$ -wave symmetry of the cuprate gap is included in Eq.3.1.5 through the  $k$ -dependent term  $\Delta_{\hat{p}}^2$ , the vortex cores are still assumed to be circular with either the Gaussian or Bessel function  $F(u)$  term discussed above. Berlinsky *et al.*[4], however, included the effects of  $d$ -wave pairing symmetry on the vortex cores in a GL approach. They found a complicated order parameter distribution that was fairly sensitive to the initial parameters that govern mixing of the  $s$  and  $d$ -wave order parameters. The magnetic field distribution was not calculated in their work, but would likely include effects from  $d$ -wave order parameter near the vortex cores. The model, however, is not suitable for fitting of experimentally measured magnetic field distributions because of the numerous unknown initial GL parameters in the theory.

Finally, Ichioka *et al.* have calculated the density of states, order parameter, magnetic field distribution and magnetic field dependence of the vortex core using Eilenberger equations[34]. These equations are highly non-trivial to solve, but include all higher order nonlocal and non-linear effects and should be valid at all temperatures and magnetic fields. The authors show that for  $b > 0.15$ , the lowest energy vortex lattice configuration for a  $d$ -wave superconductor is a square lattice oriented away from the crystal lattice axes (their calculations only compared a  $\theta=0$  or  $\pi/4$  rotation away from a crystal axis). The Fourier components of the magnetic field  $B(\vec{G})$  are

shown to be highly dependent on magnetic field, as is the vortex core radius.

### 3.1.4 Vortex Lattice States

The models presented above assume a perfectly long-range ordered vortex lattice. The lattice assumes its low-energy hexagonal configuration due to the balance between the vortex-vortex repulsive forces and the pressure from the magnetic field density. In this picture, temperature modifies the field distribution primarily by changing the values of  $\lambda_{ab}$  and  $\xi_{ab}$ . In real superconductors, however, disorder is also present, even in small quantities, and leads to a transition at higher field to glassy behaviour. The role of temperature also modifies the vortex lattice, leading to a dramatic transition to a melted vortex state. Reviews on these subjects are found in Refs. [38, 2, 5].

#### Thermal fluctuations

Thermal fluctuations are large in high temperature superconductors, mainly because of the high  $T_c$ 's that can be attained. At high temperatures, the thermal energy  $k_B T$  becomes comparable to the elastic energy, given by  $\epsilon_L$ , where  $\epsilon_L$  is the line energy. The vortex lattice then undergoes a transition to a liquid, where the flux lines are disordered, and can be entangled. The liquid state leads to a decrease in the second moment of the magnetic field distribution, as measured by  $\mu^+$ SR and the transition is marked by a discontinuous jump in thermodynamic quantities such as the magnetization or specific heat.

At higher temperatures, both conventional and unconventional superconductors often show a “peak” effect in magnetization measurements. This peak effect, a jump in the critical current, was originally associated with a softening of the vortex lattice (a

decrease in the elastic shear modulus  $c_{66}$ ), whereby the shearing energy of the lattice decreases faster than the pinning energy, allowing the lattice to rearrange itself to take better advantage of pinning centers[?]. More recently, small angle neutron scattering in niobium has pointed to an association between this peak effect and vortex lattice structural transitions ??.

The effect of thermal fluctuations on the vortex lines can be described by the Lindeman criterion. In this case, one would expect the displacement correlation function  $\langle u^2 \rangle = \langle [u(r) - u(0)]^2 \rangle$  (here  $u(r)$  is the displacement of the vortex line at  $r$  from its equilibrium position) to grow linearly with temperature[?], such that:

$$T/T_m = \frac{\langle u^2 \rangle}{C_L^2 a^2}. \quad (3.1.7)$$

$C_L$  is defined by the Lindeman criterion at  $T=T_{melt}$ :

$$\langle u^2 \rangle = C_L^2 a^2 \quad (3.1.8)$$

where  $a$  is the intervortex spacing. Empirically, it is found that  $C_L \approx 0.1 - 0.2$ .

### Effects of Disorder

Disorder also modifies the vortex state phase diagram of superconductors. Early arguments by Larkin and Ovchinnikov showed that the presence of even a minute amount of disorder in a crystal should destroy perfect translational order in systems in less than four dimensions[28, 29], on a length scale  $R_a$ :

$$R_a = \frac{c^2 a^4}{V^2 \rho_0^2} \quad (3.1.9)$$

where  $c$  is an elastic constant,  $V$  is a pinning energy, and  $\rho_0$  is a density of pinning sites. For a finite  $V$ ,  $R_a > 0$ , implying there is always a finite length scale over which

long-range order decays and that a well ordered vortex lattice could not exist since all superconductors have residual disorder. Instead a glassy phase at low temperature should give way to a liquid state at higher temperature, due to melting, in a smooth crossover. However, neutron scattering showed that the low temperature-low field phase exhibits Bragg peaks, and specific heat and magnetization measurements that the crossover with increasing temperature is first order. Thus disorder could not cause a transition in the vortex lattice to a glass at low temperature and magnetic field.

Instead Giamarchi and Le Doussal proposed the existence of a “Bragg Glass” [15, 2], where the effects of disorder were not as strong as predicted by earlier work. They showed that weak disorder modifies the linear growth of  $\langle u(r) \rangle$ , to  $r^{2/3}$  for  $R_l < R_a$ , and to logarithmic at large  $r > R_a$ . Therefore the translational correlation function  $C(r)$ , a measure of the lattice’s long range order, decays as a power law for large  $r$ :

$$C(r) = e^{iG_0[u(r)-u(0)]} = r^{-A} \quad (3.1.10)$$

where  $G_0$  is the first reciprocal vector of the vortex lattice, and  $A$  some constant near 0.22. Figure 3.1 shows how  $u(r)$  depends on  $r$  in the Bragg Glass.

The Larkin phase ( $r < R_l$ ), the displacement correlation function does not exceed  $\xi^2$ , and the vortex lines sample the random pinning sites within the width of the vortex lines (core radius  $\approx \xi$ ). In the Random Manifold regime ( $R_l < r < R_a$ ),  $\langle u^2 \rangle$  rises to  $a^2$ . Here the lines individually move about to take advantage of pinning sites without “bumping” into one another. For  $r > R_a$ , the growth in  $\langle u^2 \rangle$  is logarithmic, and dislocations do not form, such that quasi-long range order survives. For the magnetic fields of interest in this thesis,  $R_l \ll a$  and  $R_a \gg a$  [16].

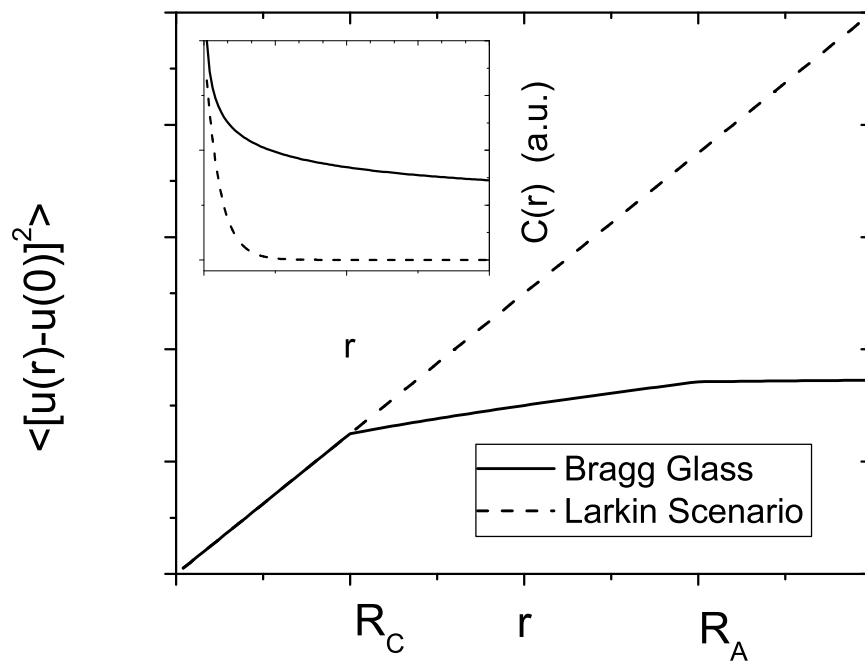


Figure 3.1: The displacement correlation function grows linearly below  $R_l$  and logarithmically above  $R_a$  in the Bragg Glass phase of the vortex state. Inset:  $C(r) = e^{G_0 u(r)}$  versus  $r$ , showing the algebraic decay in the Bragg Glass model.

### Effect of Bragg Glass on Magnetic Field Distribution

The simplest derivation of the effects of the disorder and thermal fluctuations on the field distribution can be found as follows. In the derivation of  $B(r)$ , the vortex line location  $\vec{r}_v = \vec{r}_0 + \vec{u}(\vec{r})$ , where  $\vec{r}_0$  is the equilibrium line location in the absence of disorder. Then the average over disorder is calculated as follows:

$$B(r) = \langle \sum_{\vec{r}_v} \sum_{\vec{G}} b(\vec{G}) e^{i\vec{G} \cdot \vec{r}_v} \rangle \quad (3.1.11)$$

where  $\langle \dots \rangle$  is a spatial average over disorder. Then:

$$\langle e^{i\vec{G} \cdot \vec{r}_v} \rangle = e^{i\vec{G} \cdot \vec{r}_0} \langle e^{i\vec{u}(\vec{r}) \cdot \vec{G}} \rangle \quad (3.1.12)$$

and

$$\langle e^{i\vec{G} \cdot \vec{u}(\vec{r})} \rangle = 1 - \langle \frac{(\vec{u} \cdot \vec{G})^2}{2} \rangle + \dots = \langle e^{\frac{\vec{G} \cdot \vec{u}(\vec{r})}{2}} \rangle, \dots \quad (3.1.13)$$

Thus,

$$B(r) = \langle \sum_{\vec{r}_0} \sum_{\vec{G}} b(\vec{G}) e^{i\vec{G} \cdot \vec{r}_0} e^{(\vec{G} \cdot \vec{u}(\vec{r}))^2} \rangle \quad (3.1.14)$$

Therefore Eq. 3.1.14 shows that to properly account for disorder in the Bragg Glass regime, the magnetic field distribution must be calculated self-consistently by averaging over the disorder term  $u(r)$  over the three different regimes, Larkin, RM, and logarithmic. This calculation has not been performed to my knowledge and is beyond the scope of this thesis.

## 3.2 Anomalous Magnetism and Superconductors

In this section, I examine various theories of high-temperature superconductivity and their prediction for the vortex state. Their common thread is an attempt to explain

the novel high-temperature “pseudo-gap phase” and the proximity in the phase diagram of the antiferromagnetic and superconducting phases that all high- $T_c$ 's have in common (see Chapter 2). Two classes of vortex state theories are discussed: the SO(5) theory which predicts the appearance of spin magnetism across the phase diagram, and various slave-boson theories which exhibit orbital antiferromagnetism.

### 3.2.1 Spin Antiferromagnetism

S.C. Zhang's SO(5) theory combines superconductivity and antiferromagnetism[57]. Zhang notes that two energy scales characterize high- $T_c$ 's,  $J$ , the spin-spin exchange energy, and a lower temperature associated with the formation of and competition between the AF and SC states. He formulates a Hamiltonian constrained by symmetry arguments that include the SO(3) AF and U(1) SC symmetries. A five dimensional “superspin” operator is constructed from two components of the SC order parameter (phase and amplitude of  $\Psi$ ) and the three spatial components of the AF order parameter. This superspin then has finite amplitude below a high-energy  $J$  temperature and rotates into the AF sphere (SC plane) for  $\mu < \mu_c$  ( $\mu > \mu_c$ ), where  $\mu$  is the chemical potential.

The characteristics of the system can be tuned with a single parameter  $\mu$ . The high energy scale is then associated with the formation of “Cooper” pairs, which condense into a “solid” AF near half-filling ( $\mu=0$ ). As holes are added, the AF solid melts to a superconductor above a critical value of  $\mu_c$ . At  $\mu_c$ , the SO(5) symmetry is exact. In the region near  $\mu_c$ , the system can be in a state of microscopically coexisting SC and AF, exhibit stripe-like behaviour, or spin-glass behaviour in the presence of disorder. Regardless, finite AF correlations are expected to survive near the critical

doping concentration.

Arovas *et al.*[3] constructed a GL free energy based on competing antiferromagnetic and superconducting order parameters and the SO(5) model. They showed that in the vortex cores, antiferromagnetism may appear. Qualitatively, antiferromagnetism can appear where the superconducting order parameter is reduced, in this case in the vortex cores. The authors discussed the possibility of measuring this effect with  $\mu^+$ SR and neutron scattering, predicting a step or multiple steps (depending on correlations between vortices) in the magnetic field distribution and a broad peak in the scattered neutron count at the antiferromagnetic wavevector  $q_{AF}$  (see Chapter 4).

### 3.2.2 Orbital Antiferromagnetism

A class of theories that have generated considerable interest involve some degree of separation of spin and charge. Generally, electrons separate into quasiparticles carrying spin (spinons) and charge (chargons). This novel idea has been shown to predict a number of interesting physical phenomena, such as a high temperature spin gap and antiferromagnetism.

For instance, Hsu, Marston, and Affleck[19, 21, 49] and Kotliar[?] suggested, based on spin charge separation, that a staggered flux phase (SFP) may exist in the slightly doped cuprates. The two-dimensional one-band Hubbard model (in the large  $U/t$  limit) can yield circulating currents of charge carriers around Cu-O planes in the unit cell. Hsu *et al.* calculated the orbital currents and magnetic fields at various positions in the unit cell, and predicted the appearance of magnetic fields of order 10-100 G, depending on the position of the probe and the details of the wavefunctions

used in the calculation.

Later, in a theory of the vortex core also based on the Hubbard  $t - J$  model in the  $SU(2)$  formulation, Lee and Wen predicted a SFP in the vortex cores of underdoped cuprates[53, 31]. Above  $T_c$ , Lee and Wen found a spin-gap phase which they identified with the pseudo-gap. Below  $T_c$ , the system is a pure  $d$ -wave superconductor away from the vortex cores, but a SFP is “frozen” inside the vortex cores. Near  $H_{c2}$ , they predicted the appearance of quasi-static AF fields of order 10 G in the vortex cores. Kishine *et al.*[22] have also shown that this model can explain STM measurements by Hofmann *et al.*[?].

Does this theory predict AF cores??? Franz and Tešaniović developed a related theory in the  $U(1)$  symmetry to analyze vortex core STM measurements. They assume a decomposition of the electron into a spin and charge quasiparticle, with single occupancy enforced by a  $U(1)$  gauge field. They show that holon vortices, with a unit of quantum flux, can have a spin gap because the holon amplitude goes to zero in the holon vortex cores.

### 3.3 Evolution of $\text{Cu}^{2+}$ spin magnetism with hole doping

talk about stripes theory... Emery and Zhang also.

## 3.4 Conclusion

In this chapter, the theory of the vortex state field distribution has been reviewed. Neglecting nonlocal corrections, the GL field distribution is expected to best describe the measured field distribution in type-II superconductors. The addition of predicted vortex state antiferromagnetism can modify this field distribution. Such modifications and measurements of antiferromagnetism will be discussed in chapter 5. In the following chapter, experimental methods for probing the vortex and Meissner state are presented.

# Chapter 4

## Experimental Probes of Magnetism in Superconductors

In this chapter, the three experimental methods used in this thesis, magnetometry, transverse and zero field muon spin rotation, and magnetic neutron scattering, will be reviewed.

### 4.1 SQUID Magnetometry

Squid magnetometry can measure the bulk magnetization of a small sample. The SQUID magnetometer used in this experiment is a split coil Quantum design SQUID, with a base temperature of  $T = 4.2$  K (for greater than 4 hour operation) and a maximum applied field of  $\mu_0 H = 5.5$  T. Figure ?? shows the set up of the coil. The sample is moved through the coil and the voltage across the coil leads is measured with a SQUID at various intervals (50 points for this experiment). A “point-like” sample generates a voltage versus position signal seen in figure 4.1. The magnetometer fits the voltage signal to a known function describing the movement of a point like source, with calibration factors due to coil size and diameter, and calculates a magnetization.

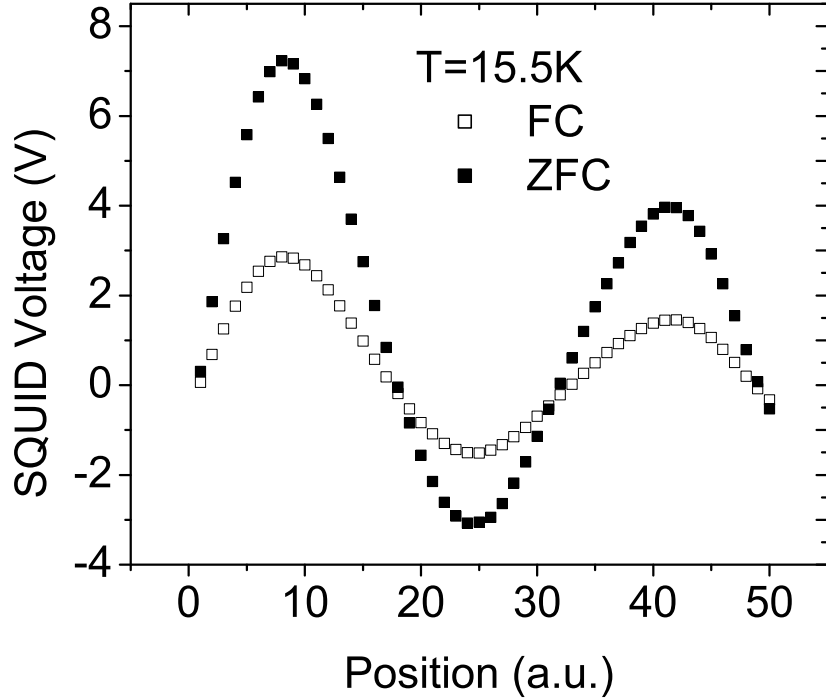


Figure 4.1: SQUID signal *vs* position in the pick up coil in  $\text{YBa}_2\text{Cu}_3\text{O}_{6.50}$  at  $T= 15.5$  K. The asymmetric tail about the center (25 a.u.) is a signal of pinning in the sample. The pinning is greatest in the zero field cooled (ZFC) run compared to the field cooled (FC) run.

Pinning, a sample that is not centered in the coil, flux creep and other effects can lead to a distortion of the voltage signal. Generally, pinning of flux lines inside the superconductor will change the signal at the tails, as seen in figure 4.1. Flux creep can add a sloping background to the magnetization signal as the sample sweeps through the coils, shown in figure 4.2.

Irreversibility lines in the vortex phase diagram can be measured in a superconductor, by zero field cooling and field cooling the sample. Irreversibility occurs due to

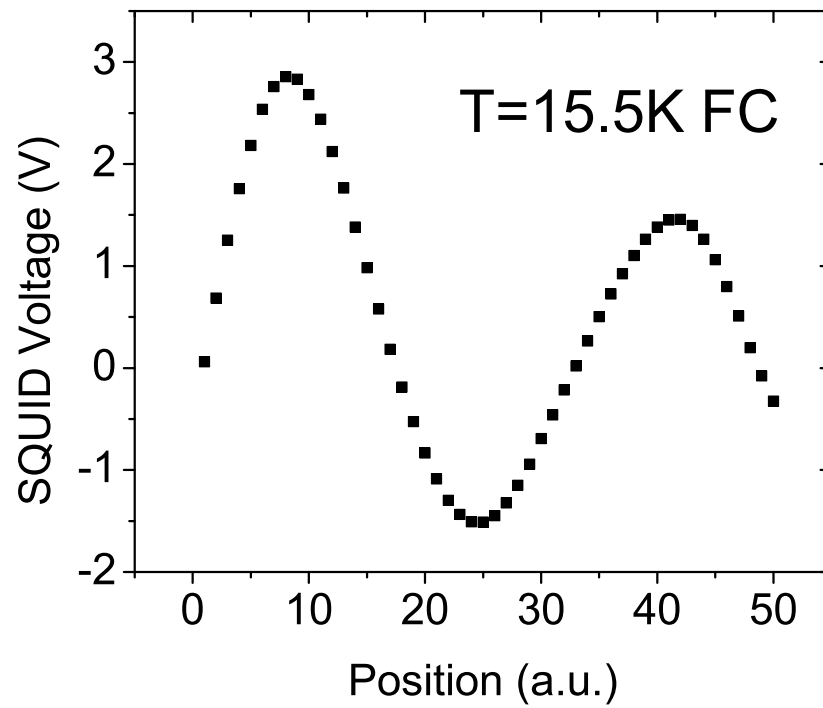


Figure 4.2: Field cooled SQUID signal *vs* position in  $\text{YBa}_2\text{Cu}_3\text{O}_{6.50}$  Flux creep during the measurement can yield a sloping background.

pinning in the sample, and is marked in the magnetometer signal by a sharp decrease in the fitting of the SQUID voltage signal. Careful measurements of the magnetization in the same magnetometer has measured a first order transition and jump in the magnetization in optimally doped  $\text{YBa}_2\text{Cu}_3\text{O}_{opt}$ [?]. Generally, most measurements of magnetization that show small first order jumps are performed by scanning Hall methods[?].

## 4.2 $\mu^+$ SR measurements

Muon spin rotation is a sensitive measure of bulk magnetism in materials. In the case of superconductors, the muon polarization signal can reveal whether in an applied field bulk superconductivity is present and measure the magnetic field distribution due to the vortex lattice, and in zero field measure small internal magnetic fields due to antiferromagnetism or anomalous spin or orbital magnetism.

The muon is a lepton with a rest mass 206 times the electron mass, spin 1/2, and a magnetic moment of  $0.0048 \mu_B$ . After a mean lifetime of  $\tau_{mu} = 2.2\mu\text{s}$ , the positive muon decays into a positron and two neutrinos -  $\mu^+ \rightarrow e^+ + \nu_e + \nu_\mu$ .

A beam of nearly 100% polarized muons are implanted one at a time in the sample. The implantation time (“start time”) is measured with a muon scintillator and photomultiplier. The muon thermalizes in less than 1 ns and, in  $\text{YBa}_2\text{Cu}_3\text{O}_{6+x}$ , is believed to bond to an oxygen. The muon spin precesses in the local magnetic field at the muon site until it decays into a positron. The positron’s momentum is directed preferentially along the muon spin at the time of decay. Positron scintillation counters, arrayed around the sample, measure the positron decay and its time relative to the start signal. Approximately 20 million muon decay events are counted in a

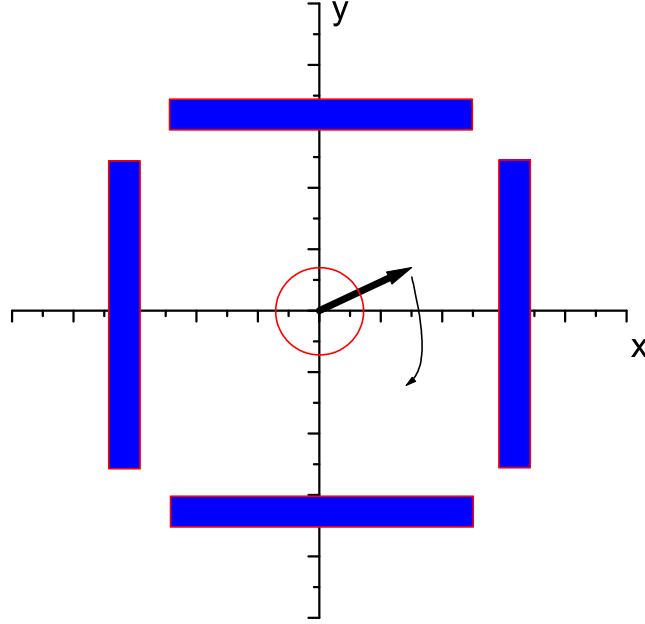


Figure 4.3: Schematic of experimental set up for 4 positron counters (dark boxes) surrounding sample (circle). Here the muon beam and applied magnetic field points into the page. The muon spin (straight arrow) precesses around the magnetic field at the Larmor frequency, sweeping by each of the counters.

high statistics measurement of the muon spin polarization. Thus, for each positron counter a histogram of muon decay events as a function of time is collected. Figure 4.3 shows schematically the experimental set up for transverse field  $\mu^+$ SR.

Figure 4.4 shows the raw spectrum from a single counter at early times. The data is taken in  $\text{YBa}_2\text{Cu}_3\text{O}_{6.50}$  in a magnetic field  $\mu_0 H = 1$  T and at  $T = 2.5$  K. The data show a precession signal at the Larmor frequency  $\nu_L = \mu_0 H \gamma_\mu$ . If this data is rebinned in larger time bins, the exponential decay of the raw data is evident, as is shown in figure 4.5. Here the oscillations due to the 1 Tesla magnetic field have been binned over at early times.

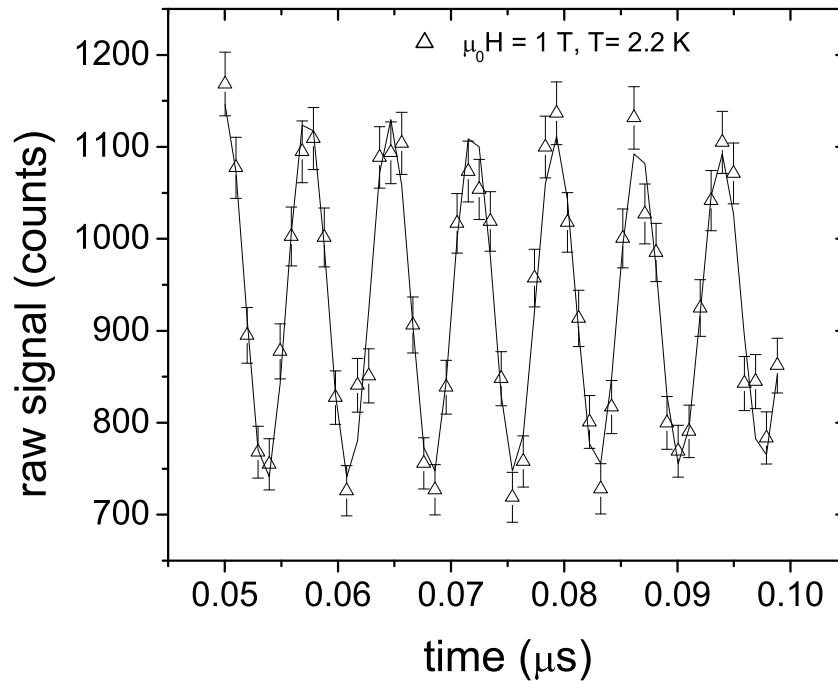


Figure 4.4: Raw counts in a single counter as a function of time, at early times, for  $\text{YBa}_2\text{Cu}_3\text{O}_{6.50}$ . The oscillations are due to the precession of the muon spin polarization in a magnetic field of  $\mu_0 H = 1 \text{ T}$ . The large number of data points in high fields makes the fitting of data in the “lab” frame very time intensive. Hence, transformations to a rotating reference frame at a frequency slightly below the main frequency of the superconductor is performed.

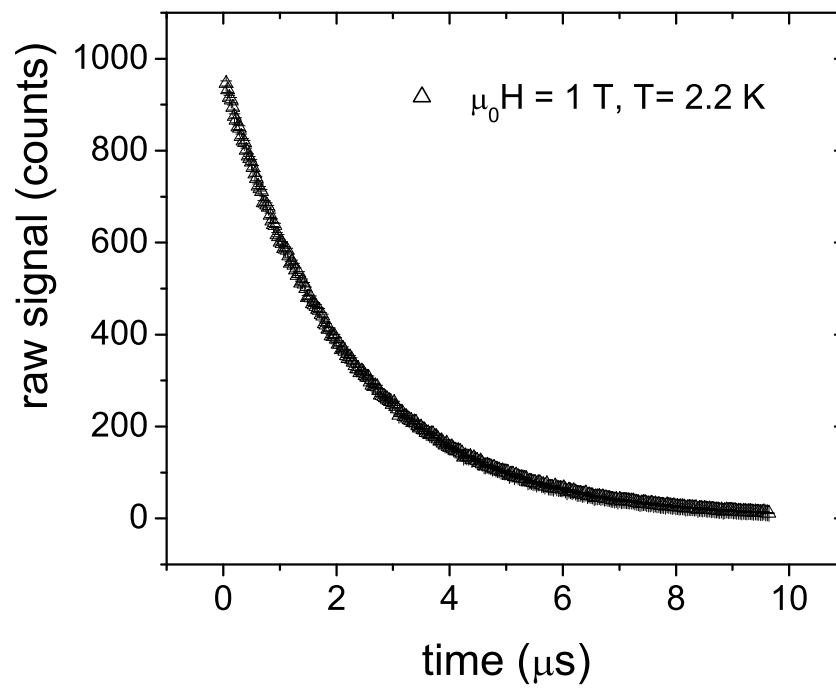


Figure 4.5: Raw counts in a single positron counter as a function of time for  $\text{YBa}_2\text{Cu}_3\text{O}_{6.50}$   $\mu_0 H = 1 \text{ T}$  and  $T = 2.5 \text{ K}$ . The oscillations at early time are binned over by selecting a time bin size larger than the oscillation period in a 1 Tesla field.

Subtracting two opposing positron counters yields an asymmetry plot. The muon spin polarization signal is given by this asymmetry signal multiplied by an asymmetry constant. This spin polarization signal can then be fit to a function that models the internal magnetism.

### 4.2.1 Transverse Field $\mu^+$ SR

In the presence of an applied magnetic field that drives the superconductor into the vortex state, TF- $\mu$ SR reveals the magnetic field distribution in the superconductor. The decay of the magnetic field away from the vortex core yields a broad distribution of magnetic fields that are sampled by the muons and hence a larger damping in the muon spin polarization signal. Figure ?? (a) shows the  $\mu^+$ SR signal in the normal state of  $\text{YBa}_2\text{Cu}_3\text{O}_{6.50}$  in an applied field of  $\mu_0 H = 1$  T; (b) in the vortex state.

The muon spin polarization signal in the vortex state is given by:

$$P_x(t) = P(0)G(t) \int_0^\infty n(\omega) \cos(\omega t + \delta) d\omega, \quad (4.2.1)$$

where  $\omega = 2\pi\gamma_\mu B$ ,  $n(\omega)$  is the magnetic field distribution in the vortex state,  $G(t)$  is a gaussian relaxation function that accounts for additional broadening due to nuclear dipole moments and lattice disorder, and  $2\pi\gamma_\mu = 135.54$  MHz/T.

When the applied field is very large ( $\mu_0 H > 0.1$  T), the muon polarization signal can be transformed into the rotating reference frame, whereby the lab frame frequency in which the polarization signal is analyzed is changed from 0 MHz to a frequency slightly below the average frequency in the superconductor. This allows for greater binning of the signal and substantially speeds up the fitting. Figs. ?? (a) and (b) are shown in the rotating reference frame.

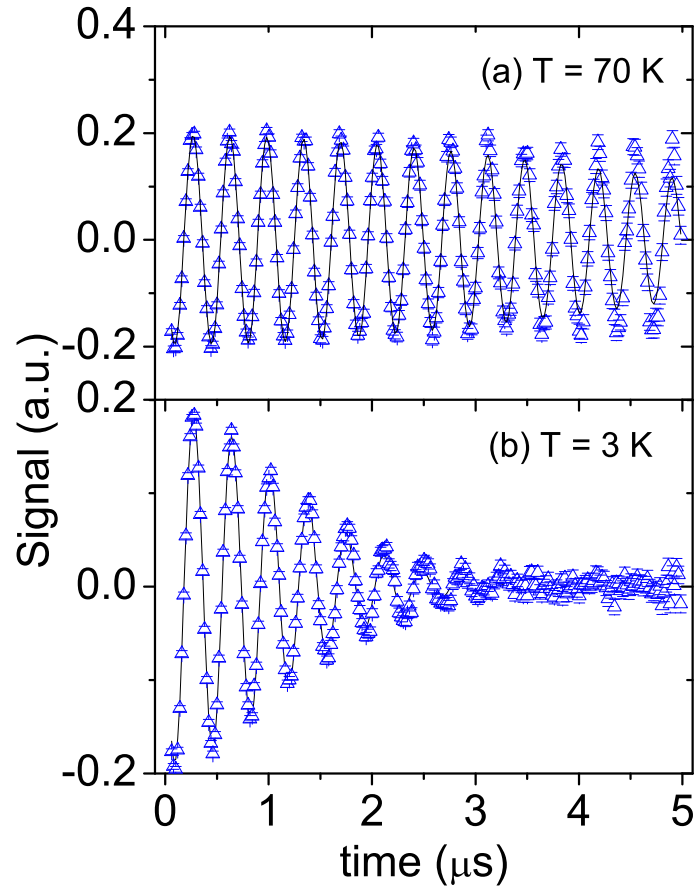


Figure 4.6: Muon polarization signal in  $\text{YBa}_2\text{Cu}_3\text{O}_{6.50}$  in a magnetic field of  $\mu_0 H = 1$  T in (a) the normal state and (b) the superconducting state ( $T = 2.5$  K). The small damping in the normal state is caused by the presence of randomly oriented nuclear spins. The additional damping in the superconducting state is primarily due to the broad magnetic field distribution of the vortex lattice.

The muon polarization signal can therefore be modelled by a choice of  $B(\vec{r})$ , for instance Eq. 3.1.4, and Eq. 4.2.1. The integral over  $\omega$  in Eq. 4.2.1 is calculated by sampling the vortex lattice reduced unit cell on a grid and calculating the contribution to the muon polarization at each site.

In the presence of a large internal magnetic fields, for instance due to antiferromagnetism, the long time transverse field signal measures the fraction of the sample where these internal fields are not present. The muon is a local probe, such that each muon senses magnetic fields within a few lattice constants. Thus muons that are not near internal magnetic fields will precess at the external, applied magnetic field. Their signal will not decay as fast as the signal due to muons that are near large internal magnetic fields.

### 4.2.2 Zero Field $\mu^+$ SR

In the absence of an external applied magnetic field, the implanted muon will precess at a frequency proportional to the local magnetic field at the muon site. In underdoped  $\text{YBa}_2\text{Cu}_3\text{O}_{6+x}$ , the large internal magnetic moments due to  $\text{Cu}^{2+}$  spins cause a magnetic field of 300 G at a muon site. A fraction of the muon signal will therefore precess at a frequency proportional to 300 G, while a smaller fraction, due to muons at sites where the magnetic field is parallel to the muon spin polarization, will decay slowly exponentially. Figure 4.7 shows the time evolution of the asymmetry signal in a oriented powder sample of  $\text{YBa}_2\text{Cu}_3\text{O}_{6.00}$

The muons signal in zero field is therefore a complicated sum of signals from each muon site, and whose strength is proportional both to the fraction of muons occupying the sites and the projection of the local magnetic field in the plane perpendicular to

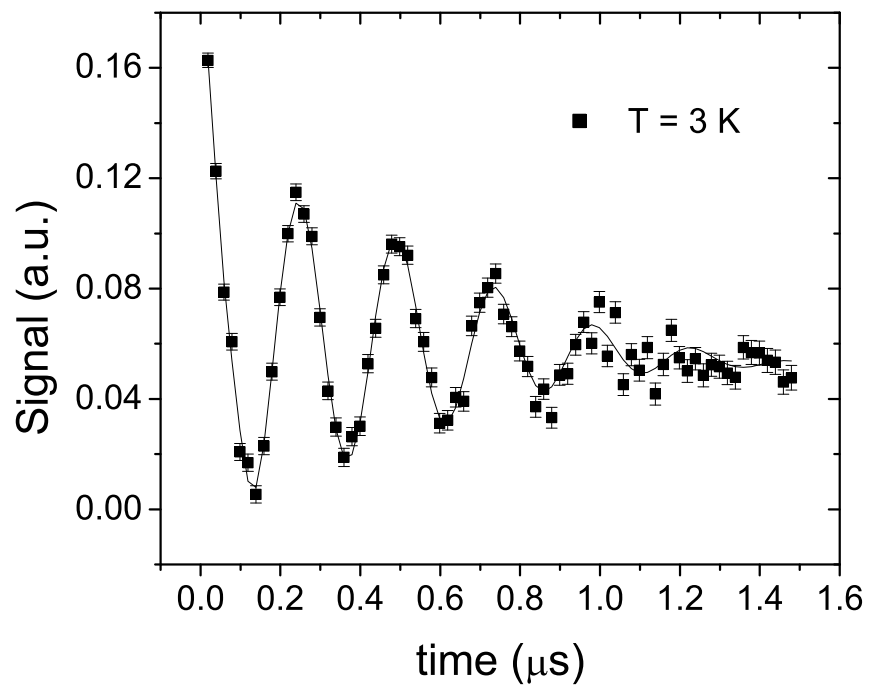


Figure 4.7: Muon asymmetry signal in GE varnished  $\text{YBa}_2\text{Cu}_3\text{O}_{6.00}$  at  $T = 3$  K. The main signal precesses at a frequency proportional to 300 G due to the antiferromagnetically aligned  $\text{Cu}^{2+}$  spins in the Cu-O planes.

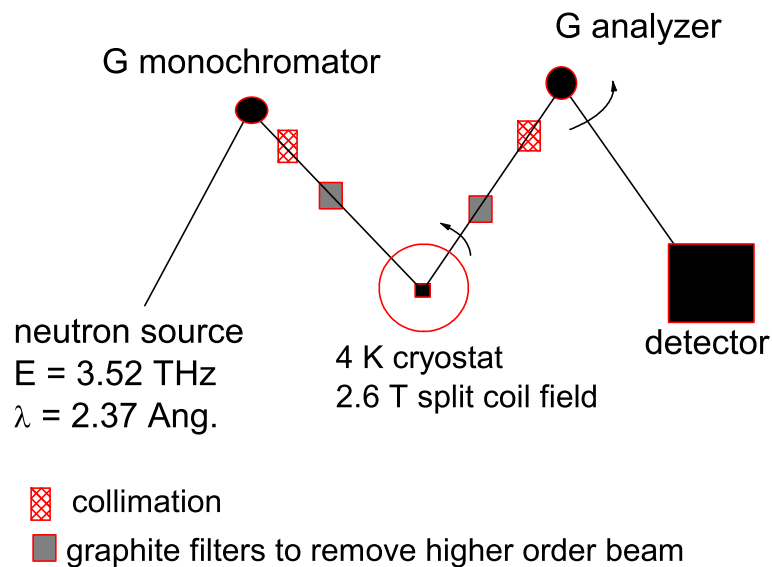


Figure 4.8: Schematic of experimental set up for elastic neutron scattering. The angle between the sample-monochromator and neutron source-monochromator selects neutron energies and  $k_i$ , the initial momentum. The analyzer rotates about the sample to choose different  $k_f$ , the final neutron momentum. The angle made between the analyzer and detector is fixed for elastic scattering. The sample is mounted in a 4 K He cooled cryostat, surrounded by a 2.6 T split coil magnet.

the muon spin polarization.

### 4.3 Elastic Neutron Scattering

Neutron scattering of magnetic materials uses the magnetic moment of the neutron ( $\mu_N$ ) as a probe of bulk magnetic order. In this section, the basic set up of neutron scattering is explained and the signal for antiferromagnetism is reviewed.

### 4.3.1 Experimental Set up

Figure 4.8 shows the experimental set up used to probe the vortex state of superconductors for antiferromagnetism. A neutron source, the AECL Chalk River reactor, provides an unfocused beam of neutrons that strike a graphite monochromator, whose angle to the beam selects a neutron energy and momentum. Between the monochromator and the sample, the beam's intensity is counted with a counter, collimated with boron-coated steel slabs, and filtered through a series of graphite filters.

The neutron beam interacts with the sample and part of the beam is Bragg scattered off the planes when the difference in final and initial momentum is a multiple of a chosen reciprocal lattice vector. The scattered beam is filtered again and collimated and strikes the analyzer where it is reflected to a detector. The final momentum can be varied by changing the angle between the sample axis (for instance the  $c$ -axis) and monochromator-sample, as well as changing the angle between the sample axis and sample-analyzer. The angle between the detector-analyzer and sample-analyzer is fixed for elastic scattering.

### 4.3.2 Magnetic neutron scattering

In neutron scattering, an incident neutron, whose spatial wavefunction is  $\Psi(\vec{k}) = A \exp(i\vec{k} \cdot \vec{r})$  interacts with a scattering system through a potential  $V(\vec{r})$  which modifies the neutron's wavevector  $\vec{k}$  and spin  $\sigma$  and absorbs energy  $E$  from or releases energy to the neutron. Hence the scattered neutron, with new wavevector  $\vec{k}'$ , energy  $E'$ , and spin  $\sigma'$ , is characterized by a different spatial wavefunction  $\Psi(\vec{k}') = A' \exp(i\vec{k}' \cdot \vec{r})$ .

The scattered neutron intensity is defined as the number of neutrons in a small solid angle  $d\Omega$  along angles  $\theta$  and  $\phi$ , whose energy is between  $E'$  and  $E' + dE$ . It is

measured by an energy-sensitive detector shown in Fig. ?? and is proportional to

$$\frac{d\sigma}{d\Omega} = \frac{1}{\Omega\Phi} \sum W_{\vec{k},\lambda \rightarrow \vec{k}',\lambda'}$$

where the transition rate from states  $\vec{k}, \lambda$  to  $\vec{k}', \lambda'$  is given by  $W$ . From Fermi's Golden Rule,

$$W_{\vec{k},\lambda \rightarrow \vec{k}',\lambda'} = 2\pi/\hbar \rho_{k'} | \langle \vec{k}'\lambda' | V | \vec{k}\lambda \rangle |^2,$$

Eq. 4.3.2 becomes:

$$\frac{d\sigma}{d\Omega} = \frac{k'}{k} \left( \frac{m_N}{2\pi\hbar^2} \right)^2 | \langle \vec{k}'\lambda' | V | \vec{k}\lambda \rangle |^2,$$

In elastic neutron scattering, energy transfers to or from the system are forbidden, and the experimenter varies the direction of the scattered and or incident neutron wavevectors. Thus, in Eq. 4.3.2,  $k = k'$ . No excitations of the system are probed, but rather the crystal or magnetic structure of the system is investigated by means of Bragg scattering.

In nuclear scattering, the neutron interacts with the lattice through the weak interaction. In magnetic scattering, the neutron's magnetic dipole moment,  $\mu_N$ , interacts with a local magnetic field  $\vec{B}$  due to lattice electrons, through an interaction potential  $V_m$ :

$$V_m = -ve\mu_N \cdot \vec{B}.$$

Unlike in nuclear scattering, where the nuclear forces are approximated as step functions, the magnetic interaction is complicated and non-central. The two contributions to a magnetic field at a distance  $\vec{R}$  from an electron with momentum  $\vec{p}$  are due to the electron dipole moment,

$$\vec{B}_{dp} = \vec{\nabla} \times \left( \frac{\mu_0}{4\pi} \frac{\vec{\mu}_e \times \hat{R}}{R^2} \right)$$

and to its momentum,

$$\vec{B}_L = - \left( \frac{\mu_0}{4\pi} \frac{2\mu_B}{\hbar} \frac{\vec{p} \times \hat{R}}{R^2} \right).$$

Bragg scattering from ions shows maxima at reciprocal lattice vectors of the crystal unit cell. In the case of the cuprates, magnetic scattering in the undoped parent compounds is peaked at  $q_{AF} = (\frac{1}{2}, \frac{1}{2}, L)$  r.l.u., where reciprocal lattice units are defined by r.l.u. =  $(\frac{2\pi}{a}, \frac{2\pi}{b}, \frac{2\pi}{c})$  and  $L$  is an integer.  $a, b, c$  are the lattice parameters of the unit cell (see chapter 2)[?]. This occurs because the unit cell in real space doubles in the  $a - b$  plane, as the copper spin order antiferromagnetically. Therefore, a search for anomalous magnetism in the Cu-O planes should start near  $q_{AF}$ .

The sharpness of the peaks near  $q_{AF}$  will be determined by the spatial correlations of the spins or orbital magnetism given rise to the scattering. Generally, a spatial (one dimensional) dependence of the magnetism given by a lengthscale  $\eta$ :

$$\vec{S}_i(\vec{r}) \cdot \vec{S}_j(\vec{r}') = e^{\frac{|\vec{r}-\vec{r}'|}{\eta}} \quad (4.3.1)$$

will lead to a width in the reciprocal space given by  $\Delta k \propto a/\eta$ , where  $a$  is the unit cell parameter in the plane.

# Chapter 5

## Results

This chapter presents results on the phase diagram, evidence of magnetism in the vortex core of  $\text{YBa}_2\text{Cu}_3\text{O}_{6.50}$  and measurements of ZF magnetism at low temperatures in  $\text{YBa}_2\text{Cu}_3\text{O}_{6.35}$

### 5.1 A phase diagram of the vortex state for Ortho-II $\text{YBa}_2\text{Cu}_3\text{O}_{6.50}$

Chapters 2 and 3 showed how the vortex state can undergo phase transitions or cross overs as temperature, magnetic field, or the density of disorder are changed. This thesis presents measurements of the vortex lattice field distribution in the vortex state at low temperatures and magnetic fields. One may therefore ask what the properties of the vortex state are in this part of the vortex state phase diagram. Measurements with a SQUID magnetometer, whose set-up is described in chapter 4, are reported here.

### 5.1.1 Squid measurements of the irreversibility line

Calorimetric and magnetization measurements have shown that a transition of the vortex lattice from a liquid to solid state can be accompanied by a change in reversible to irreversible behaviour of the lattice. Measurements on the small crucible grown samples of  $\text{YBa}_2\text{Cu}_3\text{O}_{6.50}$  have shown no evidence for a discontinuous jump in the magnetization, as may be expected if the sample undergoes a sharp melting transition.

Figure 5.1 shows the temperature dependence of the magnetization, measured on a small crystal of  $\text{YBa}_2\text{Cu}_3\text{O}_{6.50}$  with a magnetic field of  $\mu_0 H = 4$  T applied perpendicular to the  $a - b$  plane. Open  $\square$  are zero field cooled (ZFC) data, while closed  $\square$  represent data taken under field cooled (FC) conditions, where the magnetic field is applied above  $T_c$ . A small peak appears near  $T_{peak} = 20$  K, and the two signals no longer agree below  $T_{irr} = 15$  K. This signals the transition to an irreversible state due to pinning of the flux lines in the sample.

The fits to the raw SQUID data can also give additional information on the vortex state, as described in chapter 4. Figure 5.2 shows a “best fit” parameter  $R$  as a function of temperature for the data points shown in fig. 5.1. ZFC data is shown by the open triangles while FC data is given by closed  $\square$ . The onset of the decrease in the fitting parameter occurs near  $T = 22$  K while the bottom of the decrease occurs close to  $T_{peak}$ , estimated from the magnetization curve in fig. 5.1. Similarly, the ZFC signal recovers to its higher temperature value at  $T_{irr} = 15$  K. Of the three temperatures,  $T_{irr}$ ,  $T_{peak}$ , and  $T_{onset}$ ,  $T_{onset}$  marks the beginning of the transition to an irreversible state.

Similar measurements were performed at other magnetic fields. The results are shown in figure 5.3. Associating the onset of the irreversible state with  $T_{onset}$  gives an

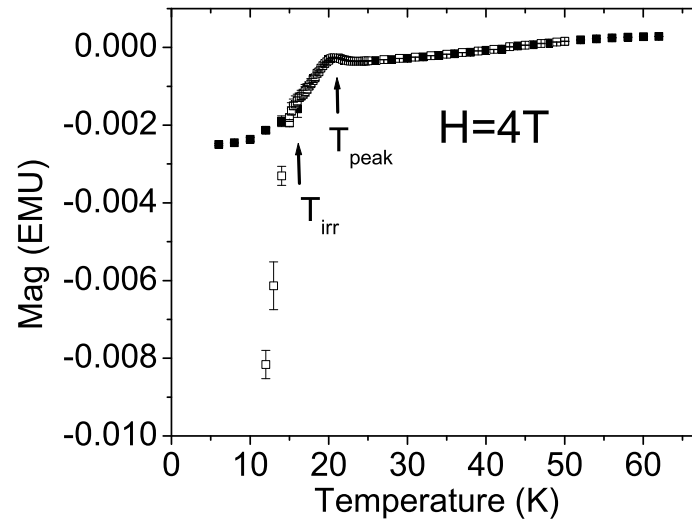


Figure 5.1: Zero field cooled and field cooled magnetization measurements in YBa<sub>2</sub>Cu<sub>3</sub>O<sub>6.50</sub> in a magnetic field of  $\mu_0 H = 4$  T perpendicular to the  $a - b$  planes. The two signals differ below  $T_{irr} = 15$  K and show evidence for a small peak near  $T_{peak} = 20$  K.

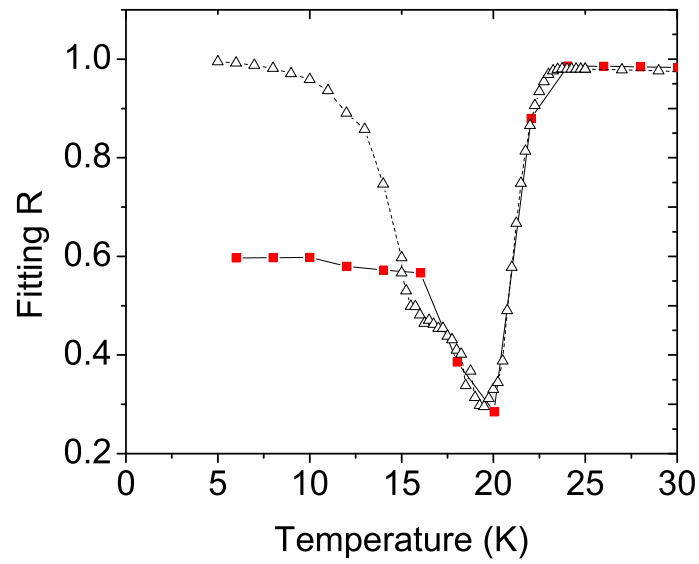


Figure 5.2: Fitting parameter of ZFC and FC magnetization data in an applied field of  $\mu_0 H = 4$  T in  $\text{YBa}_2\text{Cu}_3\text{O}_{6.50}$ . A good fit is obtained for a fitting parameter  $R=1$ . The onset of the decrease in  $R$  near  $T=22$  K signals the beginning of the irreversible state.

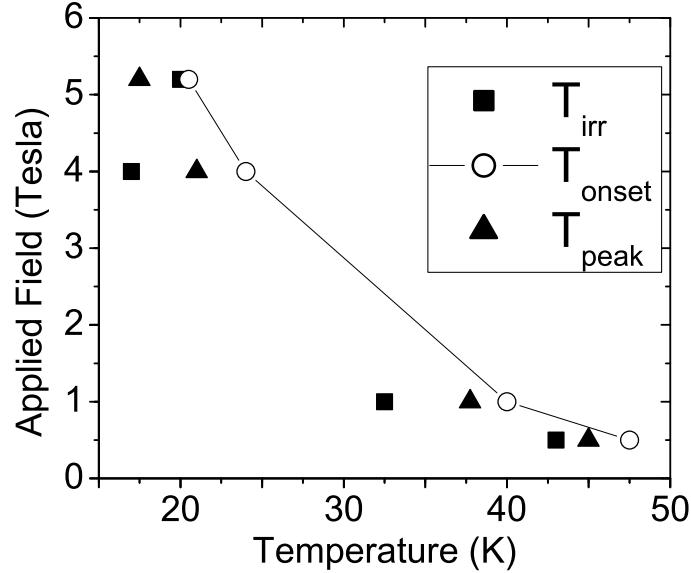


Figure 5.3: Irreversibility line measured from magnetization in  $\text{YBa}_2\text{Cu}_3\text{O}_{6.50}$ .  $T_{onset}$  signals the decrease in the fitting parameter to the raw SQUID data;  $T_{peak}$  corresponds to a peak in the ZFC and FC magnetization data; and  $T_{irr}$  occurs where the ZFC and FC magnetization data clearly diverge.

upper bound for the transition to the solid state, if one can associate the irreversible transition with the melted transition. Therefore, the results that will be presented in the following sections were taken below the melting line.

The presence of a order-disorder transition line at low temperature was not measured in the magnetization data. This is not surprising, as the only experimental evidence for such a measurement so far comes from scanning squid magnetometry and small angle neutron scattering, two methods that are more sensitive to vortex lattice order and change than SQUID magnetometry. The  $\mu^+\text{SR}$  measurements to be presented below show that at low temperatures below the irreversibility line reported in fig. 5.3, the vortex lattice has a skewness parameter close to that expected for

the field distribution of a triangular vortex lattice (skewness  $\approx 1.2$ ), which does not change abruptly either with increasing magnetic field or temperature. It should be noted that  $\mu^+$ SR is to some extent a local probe of the vortex lattice and therefore may not be very sensitive to long range disorder in the vortex lattice.

## 5.2 Vortex State magnetism in $\text{YBa}_2\text{Cu}_3\text{O}_{6.50}$

This section reports  $\mu^+$ SR and neutron scattering measurements in the vortex state of Ortho-II  $\text{YBa}_2\text{Cu}_3\text{O}_{6.50}$ . As discussed in chapter 3, various theories predict the appearance of antiferromagnetism in the vortex cores, deep in the vortex state of underdoped cuprates.

### 5.2.1 $\mu^+$ SR evidence for vortex core magnetism in Ortho II $\text{YBa}_2\text{Cu}_3\text{O}_{6.50}$

The muon polarization signal was measured at low temperatures and various magnetic fields on the M15 beamline at TRIUMF in the high-field spectrometer, BELLE, as detailed in chapter 4. The  $\mu^+$ SR signal was fit to a theoretical model using a phenomenological modified GL field distribution that includes alternating magnetic fields confined to the vortex cores. Eq. 3.1.4 was modified by adding the term:

$$B'(\vec{r}) = B(\vec{r}) \pm M e^{-(|\vec{r}|/\xi_{ab})^2/2} \quad (5.2.1)$$

where  $B(\vec{r})$  is from Eq. 3.1.4,  $M$  is a fitting parameter corresponding to the amplitude of the small alternating fields in the vortex cores, and  $\pm$  changes signs at each

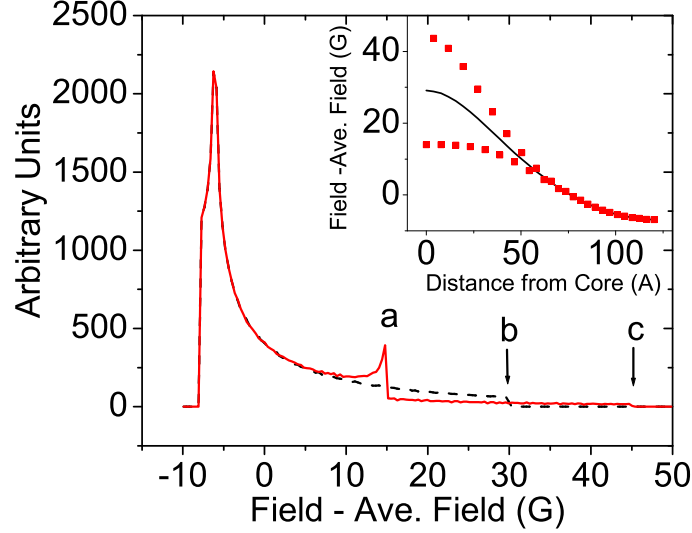


Figure 5.4: Magnetic field distribution  $n(B)$  in superconductors in an applied field of  $H=4$  T, with and without vortex core alternating fields. Solid line:  $n(B)$  calculated from Eq. 5.2.1 with alternating fields in the vortex cores ( $M = 15$  G); dashed line: field distribution without alternating fields calculated from Eq. 3.1.4 with identical values for  $\xi$  and  $\lambda$ . Notice that significant changes occur only in the high field tail. See text for further details. Inset:  $B(r)$  along a line between two vortex cores. The solid line shows  $B(r)$  without alternating fields, whereas the squares show  $B(r)$  with  $M=15$  G AF fields in the vortex core. The magnitude of the alternating fields decays away from the vortex core center.

neighbouring site  $\vec{r}$  where  $B(\vec{r})$  is calculated. The theoretical muon spin polarization function is created using Eq. 4.2.1 and 5.2.1. This modification models small alternating magnetic fields confined to the vortex core and is valid as long as  $r > L_0$ , where  $L_0$  is the distance between vortices.

The effect of  $M$  can be shown qualitatively in the magnetic field distribution. Figure 5.4 shows the effect of the vortex core alternating fields on  $n(B)$ . The dashed line shows  $n(B)$  without alternating fields ( $M = 0$  G), for typical values  $\lambda = 2450$  Å and  $\xi = 35$  Å in an applied field of  $H = 4$  T. The high-field cutoff corresponding

to the magnetic field at the vortex core center is visible at  $b$ . The modified  $n(B)$  due to the introduction of the fields of magnitude  $M = 15$  G (solid line) shows a double step in the high field tail at  $a$  and  $c$ . The lower step (at  $a$ ) is caused by additional fields in the vortex core antiparallel to the applied magnetic field  $\mu_0 H$ , whereas the upper step (at  $c$ ) originates from sites where the additional fields are aligned with the applied field. The spatial variation of the magnetic field near the vortex cores is shown in the inset. The line corresponds to  $B(r)$  from Eq. 3.1.4 without alternating fields, while the squares show  $B'(r)$  from Eq. 5.2.1 with the fields. The van Hove singularity in  $n(B)$  at  $a$  is caused by the nearly flat field distribution in the inset along the lower line of square points. These points correspond to fields aligned opposite to the applied field. Note that  $n(B)$  is unchanged away from the vortex core region, as expected.

The results presented in this chapter correspond to a sampling density of muon sites (eg., the distance between sites where  $B(\vec{r})$  is calculated) of  $Cu - Cu/10 \approx 0.4$  Å. Furthermore,  $\xi_{ab}$  is fixed to 35 Å at  $\mu_0 H = 1$  T and 45 Å at  $\mu_0 H = 4$  T.  $\chi^2$  is calculated for a given  $B_{ave} = \frac{\Phi_0}{S}, \lambda_{ab}, \xi_{ab}, M$  and other fitting parameters related to the muon polarization signal, and the parameters are varied to find the minimum  $\chi^2$ . The CERN fitting package *MINUIT* was used.

If Eq. 5.2.1 fits the muon polarization signal better than Eq. 3.1.4, an improvement in the  $\chi^2$  is expected. In figure 5.5, it can be seen that Eq. 5.2.1 does indeed significantly improve the fit. At  $T = 5$  K and  $\mu_0 H = 4$  T, a minimum in  $\chi^2$  is found for  $M \approx 15$  G.

The improvement in the fits originates in the high-field tail of the magnetic field distribution. This can be shown qualitatively by plotting the Fast Fourier transform

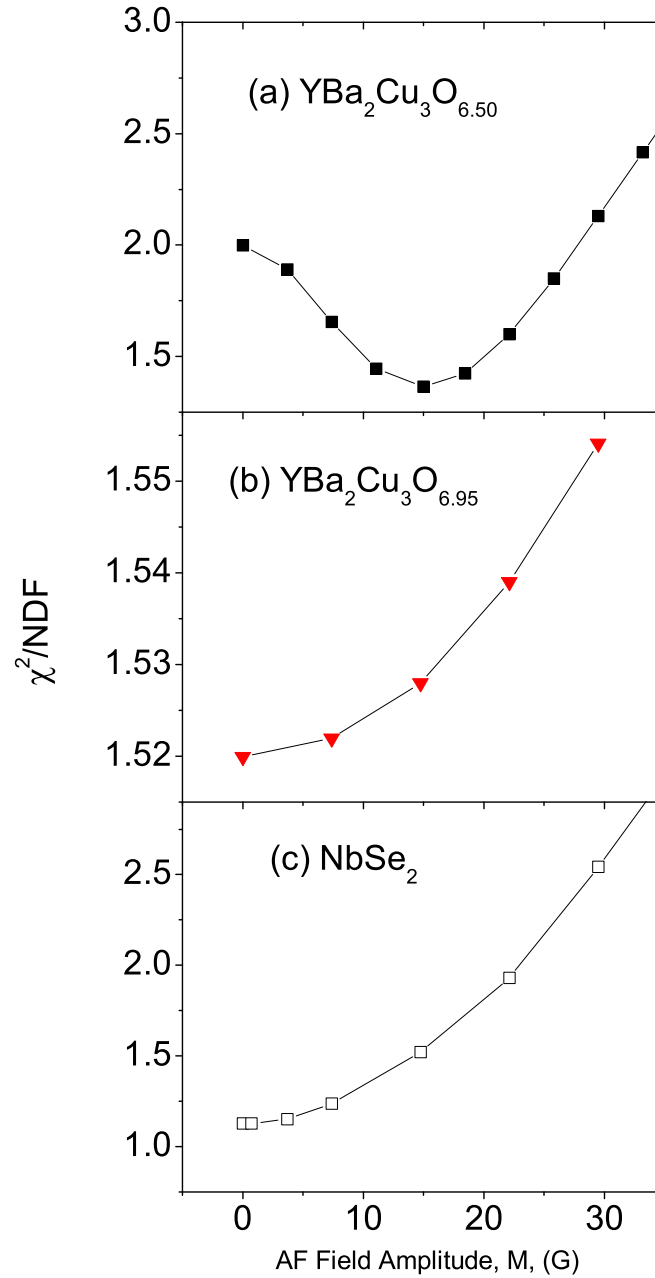


Figure 5.5: Improvement in  $\chi^2$  by varying  $M$  of fits to muon polarization signal using Eqs. 5.2.1 and 4.2.1 in (a)  $\text{YBa}_2\text{Cu}_3\text{O}_{6.50}$  (b)  $\text{NbSe}_2$  (c)  $\text{YBa}_2\text{Cu}_3\text{O}_{6.95}$ .  $\xi_{ab}$  in each panel is fixed at its  $M=0$  value.

of the fits to the data using  $B(\vec{r})$  and  $B'(\vec{r})$ , as in figure 5.6.

Various forms of the alternating field term in Eq. 5.2.1 have also been tried. Replacing the gaussian function in the alternating field term by an exponential yields a worse fit, while fitting with a second length scale for the magnetic field amplitude decay function (instead of  $\xi_{ab}$ ) provides only a marginal improvement in the fit.

Similar measurements were made at other temperatures and at  $\mu_0 H = 1$  T. Figure 5.7 show the fitted values of  $M$ . A maximum value of 18 G is found at low temperatures and decreases above  $T = 10$  K at both fields.

These results present evidence for alternating magnetic fields in the vortex cores in  $\text{YBa}_2\text{Cu}_3\text{O}_{6.50}$ . The microscopic source of the magnetism is unclear from these measurements, as is the spatial correlation of the alternating magnetism. This is because  $\mu^+\text{SR}$  does not measure long range correlation in vortices but rather a statistical average of an ensemble of vortices. Hence, any spatial distribution of magnetic fields confined to the vortex cores that yield an average field distribution described by Eq. 5.2.1 must be considered. Furthermore, changing the sample density of  $B(\vec{r})$  does not change the results much either. Again this could be a consequence of whether a vortex core magnetic field pointing up or down is centered at the vortex core, or whether each vortex core is different, leading to a sampling by the muons of all vortex core magnetic fields. This effect is in essence due to a mismatch of the vortex lattice and the crystal lattice. A further complication arises when one considers that there are likely more than one muon site in the  $\text{YBa}_2\text{Cu}_3\text{O}_{6+x}$  crystal structure (see discussion of zero field measurements in  $\text{YBa}_2\text{Cu}_3\text{O}_{6.35}$  below). Two or more muon sites would also lead to a greater sampling of alternating fields in the vortex cores.

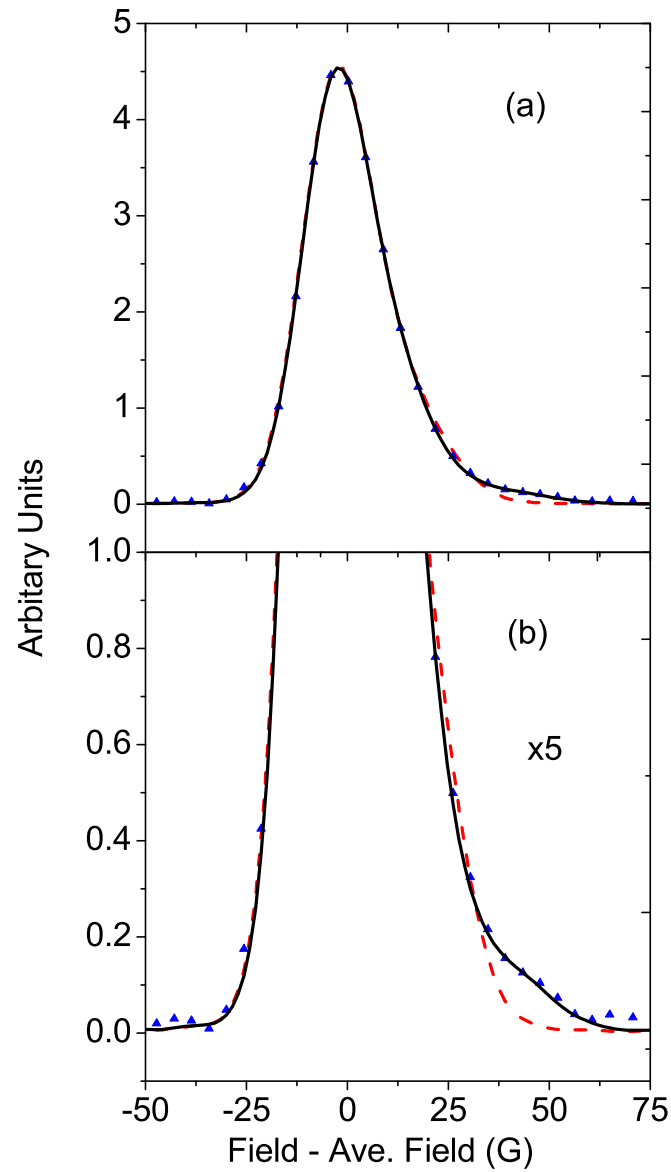


Figure 5.6: (a) Fast Fourier transform of  $\mu$ SR data (triangles) and fit (solid line) in Fig. ?? and of the best fit to Eqs. 3.1.4 and 4.2.1 without alternating fields (dashed line). (b) The high-field in greater detail. Notice the improved fit in the high field tail due to the alternating fields, corresponding to the vortex core area.

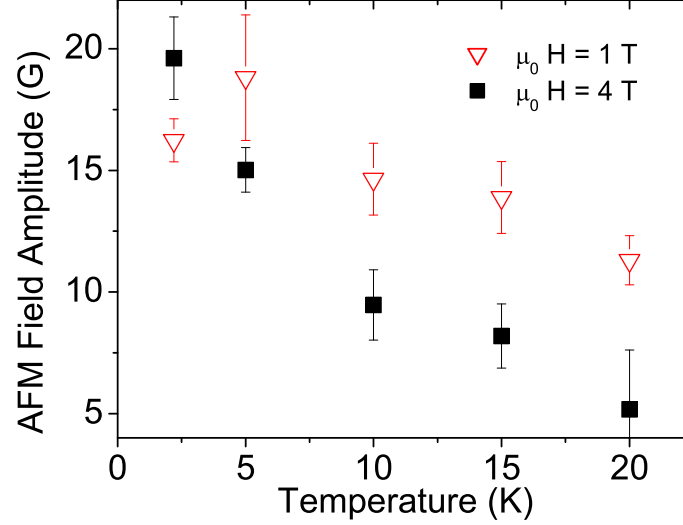


Figure 5.7: Amplitude of vortex core alternating magnetic fields measured by  $\mu$ SR *vs.* temperature, for applied fields of  $\mu_0 H = 1$  T (nablas) and  $\mu_0 H = 4$  T (full squares).

### 5.2.2 Elastic neutron scattering in Ortho-II $\text{YBa}_2\text{Cu}_3\text{O}_{6.50}$

Neutron scattering is a second experimental method that is sensitive to magnetism in superconductors, as discussed in chapters 2 and 3. Elastic scattering measurements on a single  $\text{YBa}_2\text{Cu}_3\text{O}_{6.50}$  crystal ( volume =  $2 \text{ cm}^3$ , grown by the TZMFM) were made on the N9 neutron channel at Chalk River Laboratories. Scans were made through  $\vec{k} = (\frac{1}{2}, \frac{1}{2}, L)$  for  $L = 0, 2, 4$  in reciprocal space. Three filters were used to filter out higher order scattering, and nearby Bragg peaks (1,1,0) and (0,0,6) were monitored as the magnetic field was turned on and off to ensure that the sample did not rotate or shift in the magnetic field gradients.

Results of a scan through  $(-\frac{1}{2}, -\frac{1}{2}, L = 0)$  are shown in figure 5.8 (a) and (b).  $L = 0$  corresponds to little antiferromagnetic coupling between neighbouring Cu-O planes. Firstly, our high statistics measurements clearly show no sharp peak at  $q_{AF}$

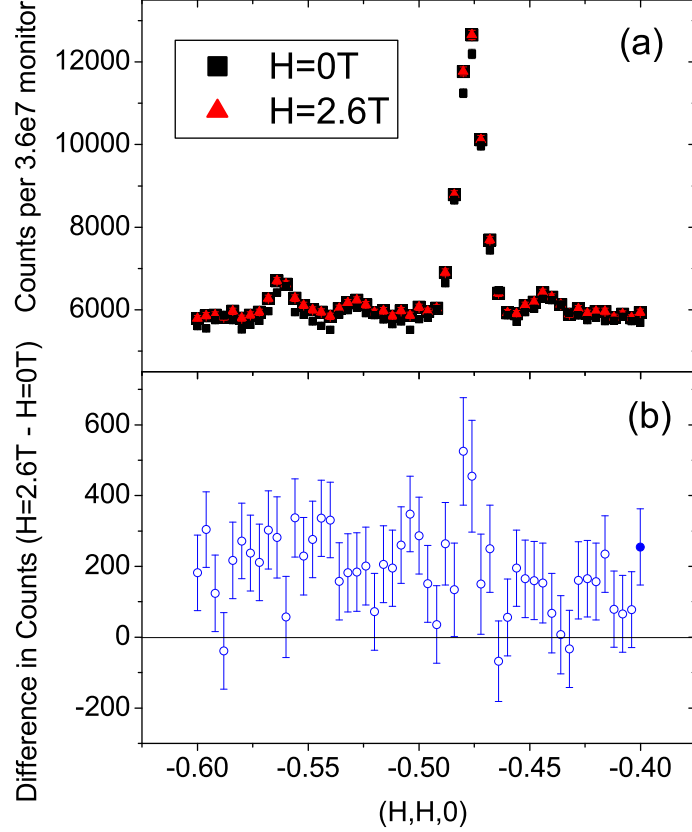


Figure 5.8: Neutron counts near  $q_{AF}$  for  $L = 0$ , in zero field (closed squares) and in a field of  $\mu_0 H = 2.6$  T (closed triangles). The peak near  $H = -0.48$  r.l.u. is a signal from an impurity phase in the crystal.

due to long ranged antiferromagnetic correlations in the planes, either in zero field or with the application of a magnetic field  $\mu_0 H = 2.6$  T. We note that the measurements of Sidis *et al.* [45] found a sharp peak at this wavevector in a  $YBa_2Cu_3O_{6.50}$  sample.

If the vortex core magnetic fields are uncorrelated from vortex core to core, then one would expect a broader signal of width  $1/\xi_{ab}$  centered at  $q_{AF}$ . As discussed earlier,  $\xi_{ab}$  is not known with great certainty. If  $\xi_{ab} \approx 35$  Å as assumed in the  $\mu^+$ SR results presented above, one would expect a reciprocal-space width of  $\Delta k = 1/\xi_{ab} * d_{ab} \approx 0.1$ . A

magnetic signal from areas outside the cores, similar to the charge density correlations measured by Hofmann *et al.* with STM [?], would result in a larger reciprocal space width.

Although there is no signal corresponding to long-range order at  $L = 0$  r.l.u., subtraction of the  $\mu_0 H = 0$  T signal from the  $\mu_0 H = 2.6$  T signal (shown in fig. 5.8 (b)) indicates an increase in scattering due to the application of the magnetic field. The short  $k$ -space range of the scans does not allow a determination of a spatial correlation range for this effect either along  $(ab)^*$  or  $c^*$  and therefore an estimate of the effective magnetic moment.

Figures ?? and ?? show a similar measurement at  $L = 2$  r.l.u. and  $L = 4$  r.l.u. respectively. The  $L = 2$  measurement indicates that the magnetic field does not increase the scattering at this wavevector significantly.  $L = 2$  corresponds to antiferromagnetic coupling between neighbouring planes. Increased scattering is observed at  $L = 4$ , however.

### 5.2.3 Conclusion

$\mu^+$ SR measurements in small  $\text{YBa}_2\text{Cu}_3\text{O}_{6.50}$  crystals have shown evidence for alternating vortex core magnetism of 18 G in applied fields of  $\mu_0 H = 1$  and 4 T. Evidence for well ordered vortex core antiferromagnetism, in an applied field of  $\mu_0 H = 2.6$  T was not found using elastic neutron scattering on large neutron crystals, at the antiferromagnetic wavevector  $q_{AF}$ . Instead, a small, broad increase in scattering in the field was measured at  $L = 0$  and  $L = 4$ .

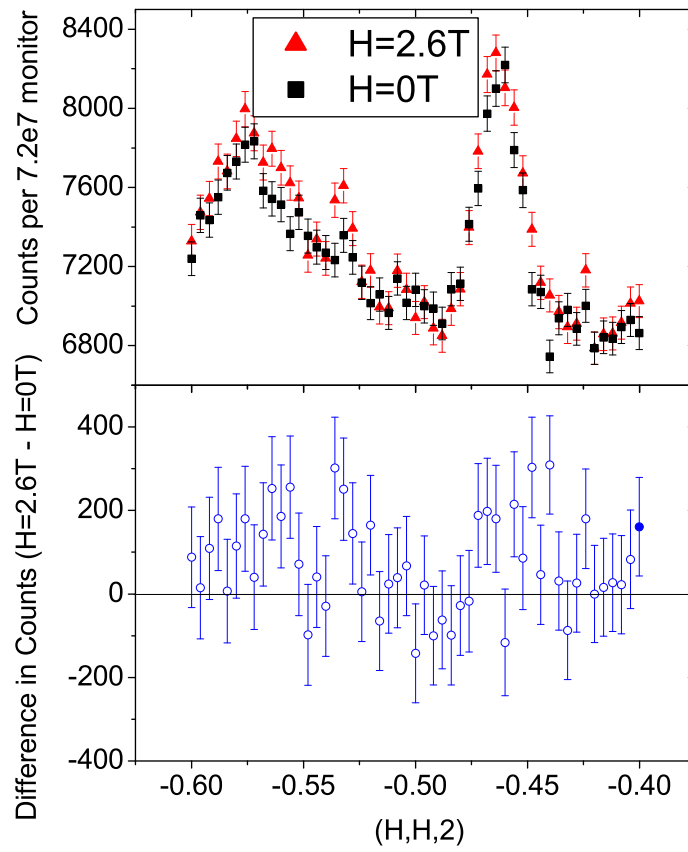


Figure 5.9: Neutron counts near  $q_{AF}$  for  $L = 2$ , in zero field (closed squares) and in a field of  $\mu_0 H = 2.6$  T (closed triangles). The peak near  $H = -0.44$  r.l.u. is a signal from an impurity phase in the crystal.

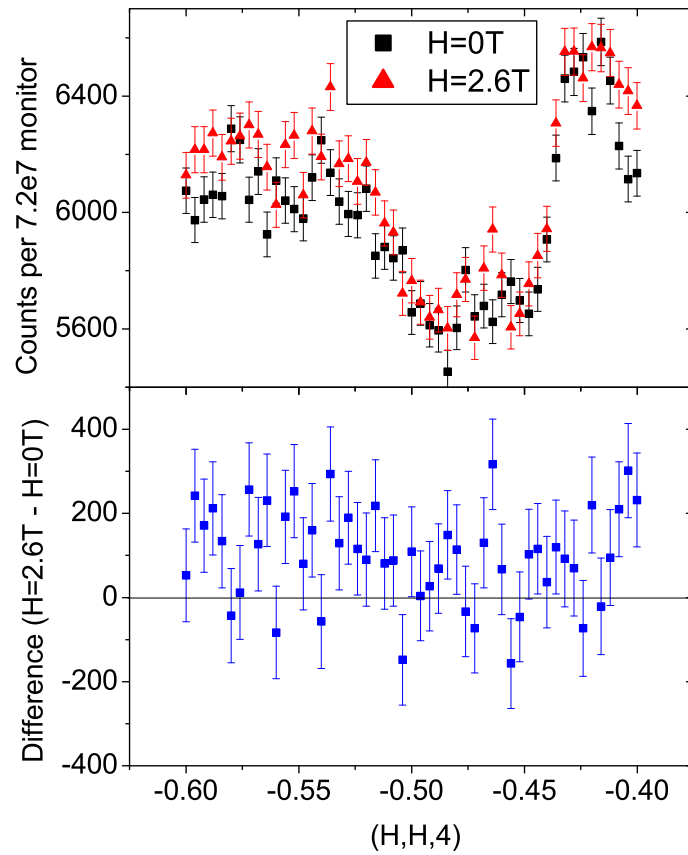


Figure 5.10: Neutron counts near  $q_{AF}$  for  $L = 4$ , in zero field (closed squares) and in a field of  $\mu_0 H = 2.6$  T (closed triangles).

### 5.3 The groundstate in Ortho-II $\text{YBa}_2\text{Cu}_3\text{O}_{6.35}$

In chapter 2, experimental evidence relating to the phase diagram near the transition from insulator to superconductor was presented. Most measurements have been made in isotropic or aligned powders. Here  $\mu^+$ SR measurements in a mosaic of  $\text{YBa}_2\text{Cu}_3\text{O}_{6.35}$  crystals are presented.

#### 5.3.1 Superconductivity in $\text{YBa}_2\text{Cu}_3\text{O}_{6.35}$

These crystals are grown in barium zirconate crucibles and are approximately 2-3 mm<sup>2</sup> each in area and 1/2 mm thick. Figure 5.11 (a) shows a SQUID measurement of the magnetisation on a small sample from the mosaic. A sharp superconducting transition occurs at  $T = 13.8$  K. Wynn *et al.* have also made scanning squid measurements on the surface of similar crystals, observing vortices[54]. Although this evidence indicates that the superconductor is a homogeneous superconductor, bulk superconductivity in these samples has not been demonstrated yet.  $\mu^+$ SR measurements either in zero field or transverse field showed no evidence for a transition to a superconducting state.

#### 5.3.2 Antiferromagnetism in $\text{YBa}_2\text{Cu}_3\text{O}_{6.35}$

Zero field measurements of the muon spin polarization signal can reveal the presence of internal magnetic fields. Figure 5.12 shows the time evolution of the muon polarization signal above ( $\Delta$ , T= 50 K) and below (closed  $\square$ , T= 3 K) a transition to antiferromagnetism. The curve through the low temperature data in fig. 5.12 is a three component fit consisting of fast and slow exponentials and a damped cosine[25].

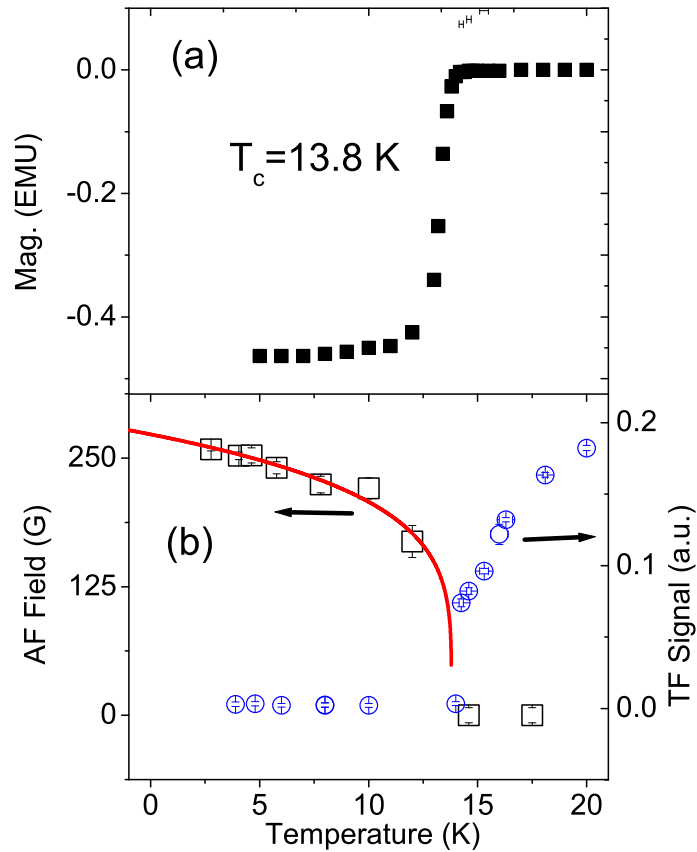


Figure 5.11: Panel (a): Temperature dependence of the magnetization in a small field as the sample is cooled through  $T_c = 13.8$  K Panel (b): Main internal magnetic field (left) and the late-time  $\mu$ SR signal amplitude as the temperature is decreased through  $T_N$ . The low temperature value of the signal indicates that the *entire* sample undergoes the transition to AF (right). The data indicate that within experimental resolution  $T_N = T_c$ . See text for details of the curve. The curve through the internal magnetic fields (left) is a fit to  $B_{AF} = B_0 * (1 - T/T_N)^\beta$ , where  $\beta = 0.22(2)$  and  $B_0 = 273(7)$  G.

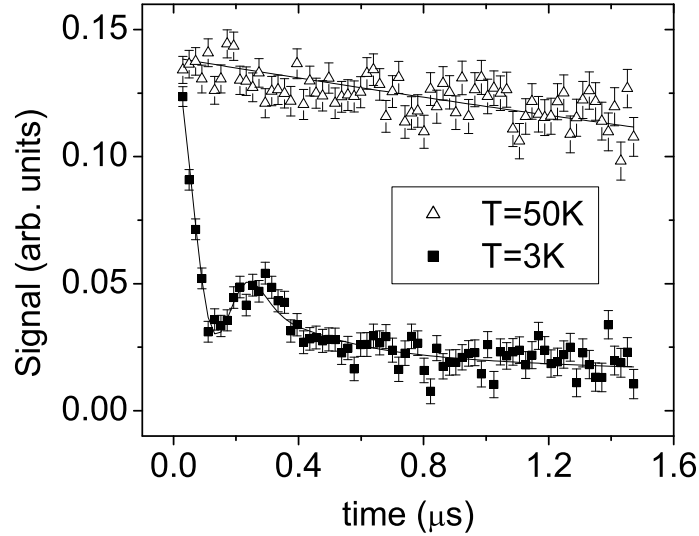


Figure 5.12: Early time  $\mu$ SR polarization signal in ZF at  $T=3\text{ K}$  (closed  $\square$ ) and at  $T=50\text{ K}$  ( $\triangle$ ). The low temperature data show an oscillation corresponding to an average field of  $273\text{ G}$  at the muon site. The rapid damping of the oscillations is caused by the presence of another magnetically inequivalent muon site and a broad distribution of fields at the sites. The curve through the data is a three component fit: a fast and slow exponential and a damped cosine. The high temperature signal is characteristic of a phase with no internal electronic fields. The curve through the high temperature data is a gaussian, whose small damping constant is caused by nuclear dipoles.

The high temperature data is fit to a single gaussian, whose small damping rate is characteristic of depolarization from nuclear fields in YBCO. The low temperature data shows that the signal is very rapidly damped, in contrast to measurements in the parent compound  $\text{YBa}_2\text{Cu}_3\text{O}_{6.00}$  where the oscillations in the muon polarization signal are much longer lived. Qualitatively, this rapid damping is caused by a broad distribution of fields at the muon site(s). The long time slow decay of the tail is partly due to the fraction of muon sites where the local field is aligned along the initial muon spin polarization.

Table 5.1: Fit to  $T = 4$  K run.

$B_{ave}$ (G)	$\Delta B$ (G)
270	68
664	181
42	25

Table 5.1: Results of fit to a high statistics run in  $\text{YBa}_2\text{Cu}_3\text{O}_{6.35}$  zero field at  $T = 4$  K with three gaussian damped cosines and a slowly relaxing exponential function.  $B_{ave} = \nu/\gamma_\mu$ , where  $\gamma_{\mu} = 135.54$  MHz/T and  $\Delta B = \sigma/2\pi$ , where  $\nu$  and  $\Delta$  are the frequency and gaussian damping rate, respectively, extracted from the fits to the data in fig. 5.13.

Data taken with high statistics (20 million events) at  $T = 4$  K reveal additional frequencies. Fig. 5.13 shows the muon polarization signal at with a finer binning. The smaller bin size and more importantly high statistics reveal an additional frequency near 9 MHz. The data is fitted to a the sum of three gaussian damped cosines and a slowly relaxing exponential function. Table 5.1 shows the frequencies and gaussian widths associated with each frequency. The 270 G field corresponds to a 10% reduction of the field at the muon site measured by Nishida, Brewer and Kiefl, reported in chapter 2. The 660 G field likely corresponds to a muon site located nearer the planes. The 42 G field is probably an artifact of the fit, as the slowly varying contribution from this frequency helps fit the long-lived signal past  $1 \mu\text{s}$  (not shown in figs. 5.12 and 5.13). Both the fits to three frequencies and a slowly varying exponential and to a fast and slowly varying exponential and a single ( 270 G) frequency yield values of the reduced  $\chi^2 \approx 1.2$ .

A fit to a model of the muon signal with a spin density wave[?, ??]ields a poorer  $\chi^2$  and does not give a consistent fit at all temperatures.

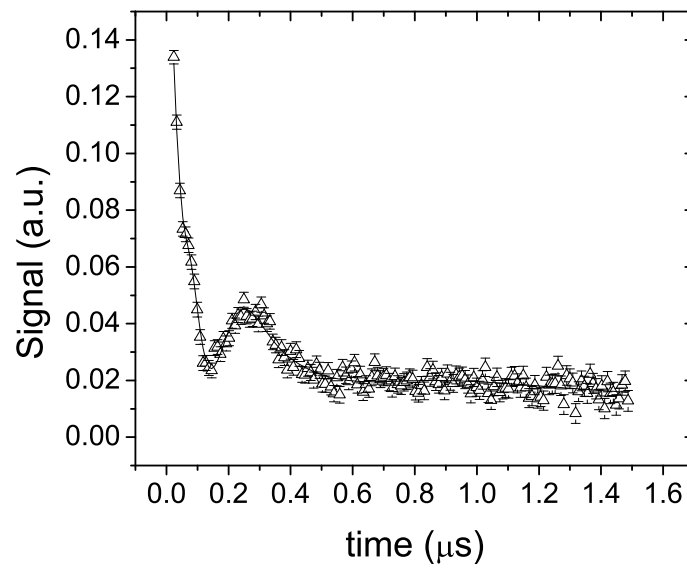


Figure 5.13: Muon polarization signal (multiplied by asymmetry) in  $\text{YBa}_2\text{Cu}_3\text{O}_{6.35}$  at  $T=4\text{K}$  in zero field, taken with 20 million events. The curve is a fit to three gaussian damped frequencies and an additional slow relaxing exponential function. The kink in the data near  $t=0.1\mu\text{s}$  reveals an additional high frequency near 9 MHz, which is binned over in fig. 5.12.

Following the temperature dependence of the 270 G field can be done by binning over the higher frequency as in fig. 5.12. The result is shown in 5.11 (b) on the left axis. The curve is a fit to  $B_{ave} = B_0 * (1 - T/T_N)^\beta$ , where  $\beta = 0.22(2)$  (in agreement with Ref. [39]) and  $B_0 = 273(7)$  G. Above  $T = 14$  K a frequency can no longer be resolved in the data, indicating that the sample has gone through a transition to a normal paramagnetic state. The large internal fields present in the sample below  $T = 14$  K mask any broadened signal from a flux lattice that may be associated with the transition to a superconducting state measured at the same temperature with a SQUID.

The sample fraction that is antiferromagnetic can also be measured with  $\mu$ SR. In the presence of an applied magnetic field that drives the sample into the vortex state, TF- $\mu$ SR reveals the paramagnetic fraction of muons that precess near the applied magnetic field. A decrease in the paramagnetic TF- $\mu$ SR signal is expected as the sample enters the antiferromagnetic state and large internal magnetic fields depolarize the late-time muon polarization rapidly. Figure 5.14 shows the late time polarization signal in an applied transverse field of  $\mu_0 H = 0.5$  T above and below  $T_N$ . The antiferromagnetism drives the paramagnetic signal that precesses at  $\mu_0 H$  to zero below the transition, indicating that *all* muons are experiencing large internal magnetic fields. The temperature dependence of the TF muon polarization signal, fig. 5.11 (b) (right axis), proves that the entire sample undergoes a transition at  $T_N$  to antiferromagnetism.

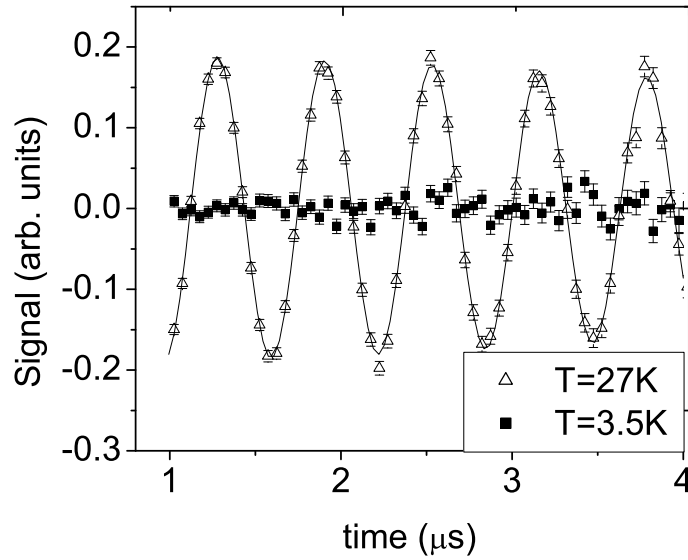


Figure 5.14: Late-time muon polarization signal at  $T > T_N$  ( $\Delta$ ) and at  $T < T_N$  (closed  $\square$ ). As the temperature is lowered through  $T_N$ , the late-time  $\mu$ SR signal decreases as the large internal magnetic field depolarize the signal rapidly.

### 5.3.3 Conclusion

$\mu^+$ SR measurements in zero and an applied field have shown that  $\text{YBa}_2\text{Cu}_3\text{O}_{6.35}$  undergoes a 100% bulk transition at  $T = 14$  K from a paramagnetic state to a low temperature “disordered” antiferromagnetic state. At the same temperature, magnetization measurements reveal a sharp transition to a superconducting state. The field at the main muon site is approximately 90% of the field measured in the parent undoped compound and the field distribution at the muon site is broad, indicating that the magnetism is perturbed from the parent compound.

# Chapter 6

## Discussion and Conclusion

### 6.1 Vortex Core Magnetism

A question of great interest is the magnitude and direction of the effective moment (spin or orbital) that could give rise to alternating magnetic fields in the vortex cores of magnitude 18 G. Two factors that need to be known are the muon site and the direction of the effective moment. Since  $\mu^+$ SR is not sensitive to an effective moment, and the muon site(s) is not known, the calculation of an effective moment is not possible.

The manner in which  $B(\vec{r})$  is calculated from Eq. 5.2.1 could in principle affect our results. The crystal lattice of copper atoms in the CuO planes is rectangular, while the reduced unit cell of the vortex lattice is hexagonal. I have verified that sampling the reduced lattice on a grid commensurate with either the crystalline lattice or the vortex lattice does not alter these results. Furthermore, because the vortex core separation is not an integer multiple of the oxygen atom spacing, the vortex cores will be centered at different locations in the CuO unit cell throughout the sample.

Hence, muons localized nearest the vortex core centre in the planes will likely see different magnetic fields depending on which vortex core they are located in. This can be simulated by sampling the vortex lattice in the calculation of  $B(\vec{r})$  on very fine intervals ( $\approx d_{Oxy-Oxy}/10$ ). Again, no effect on the results presented in this thesis is seen. Therefore, the possibility that the origin of these alternating fields in the vortex cores is due to the sampling method of the reduced unit cell is eliminated.

Furthermore, if as seems likely muons occupy more than one lattice site in the unit cell, the vortex core magnetic fields would be probed at numerous positions, both due to the incommensurability between the vortex and crystal lattice and the multiple muon sites. Both of these effects substantially complicate any estimate of moment size. If one assumes that these magnetic fields in the vortex cores are due to  $\text{Cu}^{2+}$  spins in the vortex cores, and that the orientation and size of the spins is the same as that in the undoped parent compound  $\text{YBa}_2\text{Cu}_3\text{O}_{6.00}$  a calculation of the muon site near an oxygen can be made that yields a 20 G magnetic field along the  $c$ -axis.

calculate muon site with 20G c axis.

The  $\mu^+$ SR measurement is not very sensitive to the spatial correlation of the effective moments in the vortex cores, nor their size. Neutron scattering provides a better tool for determining these properties. However, the measurements on  $\text{YBa}_2\text{Cu}_3\text{O}_{6.50}$  large crystals showed no sharp peaks near the expected wavevector,  $q_{AF}$ , as discussed in chapter 5. It must be noted that the two samples are not the same: the neutron crystal is likely more disordered, due to impurities, oxygen disorder, and homogeneity, than the small crucible  $\mu^+$ SR sample. If the vortex core magnetism is very sensitive to such disorder, then one should not be surprised to not see a magnetic signal with neutron scattering.

Another possibility is that the signal is too small and that we did not count long enough. Again it seems unlikely that this is the case. Assuming an ordered spin moment at the Cu site of  $0.65 \mu_B$ , a magnetic signal should be reduced by  $H/H_{c2}$ , the area fraction covered by vortex cores.

calculate rough size of signal we would expect from musr. mag signal times Bragg peak somewhere,

The real space correlation between neighbouring moments and between neighbouring vortex cores may also affect the size of the signal. As described in chapter 4, the size of the muon signal will decrease and broaden as the correlation length  $\eta$  decreases. Hence, the lack of peak at  $q_{AF}$  and the increase in scattering at  $L = 0, 2$  in the presence of a magnetic field may be due to magnetism in the vortex core that is uncorrelated from core to core. One would expect the width of the signal to be of order  $2\pi a/\eta = 1.0$  r.l.u. Noting that our neutron measurements were over 0.2 r.l.u. in reciprocal space, such scattering would appear constant over the range of measurement. To confirm this possibility, measurements over a wider range of reciprocal space need to be performed and at more points along  $c^*$  to determine the form factor of the scattering. Finally, I note that Lee *et al.* have made similar measurements in  $\text{La}_{2x}\text{Sr}_x\text{Cu}_2\text{O}_4$  in a field and without a field. They have observed a similar increase in scattering in a field that persists well above  $T_c$ [30].

## 6.2 Magnetism in $\text{YBa}_2\text{Cu}_3\text{O}_{6.35}$

The nature of the magnetism in this sample is unclear. As noted above, the local field at the muon site corresponds to about 90% of the field in the undoped parent

Table 6.1: (a) Stripes

$N_{AF}$	$B_{ave}$ (G)	$B_2$ (G)
8	245	83
12	268	75
16	279	68

(b) Random Disorder

Disorder Density	$B_{ave}$ (G)	$B_2$ (G)
5%	308	63
15%	295	102
25%	273	128

Table 6.1: Results of calculations on a 200\*200 grid of the dipolar magnetic fields at the  $\mu^+$  site due to Cu moments ( $0.65*\mu_B$ ) in the Cu-O planes. The  $\mu^+$  site is assumed to lie 1 Å away from the bridging oxygen O(1). In the absence of disorder or stripes, the magnetic field at the muon site is  $B = 313$  G. Part (a): Disorder induced by stripes with magnetic unit cell length  $N_{AF}$ . Moments in the stripe do not contribute to the field at the  $\mu^+$  site.  $B_{ave}$  is the average field seen at the muon site, averaged over  $N_{AF}$  stripes.  $B_2$  is a measure of the field distribution at the muon site,  $B_2 = \sqrt{\sum_i (B_{ave} - B_i)^2}$ . Part (b): Disorder due to random missing moments, averaged over 1000 configurations of random disorder introduced into the planes.  $B_{ave}$  and  $B_2$  as above.

compound  $\text{YBa}_2\text{Cu}_3\text{O}_{6.0}$ [8]. The broad distribution of fields at the muon site indicates disordered AF, but the large average field suggests a large density of magnetic moments, indicating that the small hole density in the superconducting planes has not greatly disturbed the density of moments measured in the parent compound. Possible scenarios that would explain these findings include diluted moments due to a random distribution of holes, and charge and spin stripes. Fluctuating stripes at THz energies yield the same time-averaged magnetic field at the muon site and broad field distribution, and therefore fluctuating or static stripes cannot be distinguished by the ZF- $\mu$ SR measurements.

We present two possible models of static disordered AF: a) a simple model of

two antiferromagnetically coupled planes of dipolar fields from antiferromagnetic Cu moments ( $\mu_{Cu} = 0.65 * \mu_B$ ), with static stripes. The moments in the “charge” stripe do not contribute to the field at the muon site, and the average field ( $B_{ave}$ ) and second moment ( $B_2$ ) are calculated on a  $N=200*N=200$  grid; b) two planes with Cu moments, as above, with moments randomly chosen to not contribute to the dipolar field at the muon site. In both models, the muon site is assumed to lie near the bridging oxygen (O(1))  $2.3\text{\AA}$  above a planar Cu moment, and other field contributions at the muon site, such as the hyperfine interaction are ignored. The dipolar field at this muon site due to unperturbed planes of Cu moments is  $B_{AF} = 310$  G, close to the measured field in undoped YBCO.

The results of our calculations are shown in Table 6.1. The stripes scenario with a magnetic unit cell of 16 (7 of 8 stripes with a  $\pi$  phase change at the charge stripe) is qualitatively consistent with our measurements of the reduction of the average field and broadening of the field distribution measured at the muon site. We note that  $1/N_{AF} = 0.0625$ , which is close to the estimated hole density ( $p = 0.06$ ) in this sample estimated from a parabolic relationship between  $T_c$  and  $p$ [32]. The model of random holes, on the other hand, indicates that approximately 25% of the moments must be “switched off” to achieve the reduction in average field and field broadening measured with  $\mu$ SR, much higher than in the stripes scenario due to the correlations in the stripes. Furthermore, the second moment of the field distribution in the disorder model is about twice as large as the measured moment from  $\mu$ SR. We note that  $\mu$ SR alone cannot distinguish between these two scenarios, and that using a different muon site (for instance near the planar oxygens), changes the average field and reduces the ratio of  $B_2/B_{ave}$  due to stripes or random disorder.

Evidence for a stripes model of the  $\text{YBa}_2\text{Cu}_3\text{O}_{6.35}$  magnetism comes from Mook *et al.* They report a neutron measurement of dynamic charge and spin ordering due to stripes with  $N_{AF} = 16$  in  $\text{YBa}_2\text{Cu}_3\text{O}_{6.35}$  ( $T_c = 37(10)\text{K}$ )[17]. In the much smaller, crucible-grown single crystal, a much smaller  $T_c$  and a sharper transition are observed, and there is no evidence for antiferromagnetism at high temperatures. The results presented here are, however, consistent with a stripes model with the same magnetic unit cell. The difference between these two measurements may result from the different time in the two experiments and/or from crystal growth and oxygen homogeneity.

### 6.3 Conclusion

The experimental results presented in this thesis offer evidence for anomalous magnetism in the vortex cores and bulk of underdoped  $\text{YBa}_2\text{Cu}_3\text{O}_{6+x}$ . An outstanding question in the study of high-temperature superconductivity remains an understanding of the normal state physics at low temperatures and the heavily underdoped region of the phase diagram. In  $\text{YBa}_2\text{Cu}_3\text{O}_{6.35}$  the physics of the material are still dominated by the  $\text{Cu}^{2+}$  spin magnetism which persists to a hole density of  $n_h = 0.6$ . Nevertheless, the material still shows evidence of superconductivity, despite the presence of large internal magnetic fields and the very low carrier density. In  $\text{YBa}_2\text{Cu}_3\text{O}_{6.50}$  on the other hand, superconductivity is very robust, with a  $T_c = 59\text{K}$  and no sign in zero field of large internal magnetic fields of order 300 G. However, the application of a magnetic field induces magnetism in the vortex cores. Its nature, however, is unclear, with neutron scattering results suggesting that the magnetism is not correlated over more than a few lattice constants. Whether the magnetism is of spin or orbital

origin is also unknown, and could really only be determined by neutron scattering by measuring the form factor of a magnetic signal.

Outstanding questions raised by this thesis include whether the  $\mu^+$ SR signal measured in crucible grown  $\text{YBa}_2\text{Cu}_3\text{O}_{6.50}$  exists at slightly higher or lower doping; whether it exists in larger neutron crystals; whether the superconductivity in  $\text{YBa}_2\text{Cu}_3\text{O}_{6.35}$ s indeed bulk; and how the disordered magnetism,  $T_c$ , and  $T_N$  change as the doping is incrementally changed as  $x$  is slightly increased.

# Bibliography

- [1] P. Dalmas de Réotier A. Yaouanc and E.H. Brandt, Phys. Rev. B **55** (1994), 11107.
- [2] T. Giamarchi and S. Bhattacharya, cond-mat/0111052v1 (2001).
- [3] D. Arovas et al., Phys. Rev. Lett. **79** (1997), 2871.
- [4] A. J. Berlinsky and others., Phys. Rev. Lett. **34** (1979), 409.
- [5] G. Blatter and others., Rev. Mod. Phys. **66** (1994), 1125.
- [6] F. Bouquet and others., Nature (London) **411** (2001), 448.
- [7] J.H. Brewer et al., Phys. Rev. Lett. **60** (1988), 1073.
- [8] ———, Physica C **162** (1989), 157.
- [9] ———, Physica C **162** (1989), 33.
- [10] R.J. Creswick C. P. Poole Jr., H.A. Farach, *Superconductivity*, 1 ed., Academic Press, 1995.
- [11] L.L. Miller D. Vaknin, J.L. Zarestky, Physica C **329** (2000), 109.
- [12] P. Dai et al., Nature **406** (2000), 965.
- [13] ———, Phys. Rev. B **63** (2001), 54525.

- [14] J.A. Fendrich et al., Phys. Rev. Lett. **77** (1996), 2073.
- [15] T Giamarchi and P Le Doussal, Phys. Rev. B **52** (1995), 1242.
- [16] M. Gingras, *private communication.*, 2001.
- [17] P. Dai H. Mook and F. Dogan, Phys. Rev. Lett. **88** (2002), 097004.
- [18] S. Salem-Sugui I. Abrego Castillo, L. Ghivelder, Physica C **282** (1997), 2181.
- [19] J. B. Marston I. Affleck, Phys. Rev. B **37** (1988), 2888.
- [20] M. Franz I. Affleck and M.H.S. Amin, Phys. Rev. B **55** (1997), R704.
- [21] I. Affleck J. B. Marston, Phys. Rev. B **39** (1989), 11358.
- [22] X.G. Wen J. Kishine, P.A. Lee, Phys. Rev. Lett. **86** (2001), 5365.
- [23] R.F. Kiefl J.E. Sonier, J.H. Brewer, Rev. Mod. Phys. **724** (2000), 769.
- [24] T. Kellin et al., Nature (London) **413** (2001), 404.
- [25] R.F. Kiefl et al., Phys. Rev. Lett. **63** (1989), 2136.
- [26] V.G. Kogan and others., Phys. Rev. B **54** (1996), 12386.
- [27] B. Lake et al., Science **291** (2001), 1759.
- [28] A.I. Larkin, Sov. Phys. JETP **31** (1970), 784.
- [29] A.I. Larkin and Y.N. Ovchinnikov, J. Low Temp. Phys. **34** (1979), 409.
- [30] H.? Lee, 2002.
- [31] P.A. Lee, Phys. Rev. Lett. (2001).
- [32] J.L. Loram and J.W. Tallon, Physica C **349** (2000), 53.

- [33] Z. Tešanić M. Franz, Phys. Rev. B. **63** (2001), 064516.
- [34] A. Asegawa M. Ichioka and K. Machida, Phys. Rev. B **59** (1999), 8902.
- [35] Y. Tokura M. Imada, A. Fujimori, Rev. Mod. Phys. **70** (1998), 1039.
- [36] M. Franz M.H.S. Amin and I. Affleck, Phys. Rev. B **58** (1998), 5848.
- [37] ———, Phys. Rev. Lett. **84** (2000), 5864.
- [38] T. Natterman and S. Scheidl, Adv. in Phys. **49** (2000), 607.
- [39] Ch. Niedermayer et al., Phys. Rev. Lett. **80** (1998), 3843.
- [40] N. Nishida et al., Jpn. J. Appl. Phys. **26** (1987), no. Pt. 2, L1856.
- [41] ———, J. Phys. Soc. Jpn. **57** (1988), 599.
- [42] W.N. Hardy R. Liang, D.A. Bonn, Phys. Rev. Lett. **76** (1996), 335.
- [43] Ch. Renner et al., Phys. Rev. Lett. **80** (1998), 3606.
- [44] M. Roulin et al., Phys. Rev. Lett. **80** (1998), 1722.
- [45] Y. Sidis et al., Phys. Rev. Lett. **86** (2001), 4100.
- [46] J.E. Sonier and others., Phys. Rev. B **61** (2000), R890.
- [47] ———, Phys. Rev. Lett. **83** (2000), 4156.
- [48] N. Kobayashi T. Naito, R. Nishizaki, Physica C **282** (1997), 2117.
- [49] I. Affleck T.C. Hsu, J. B. Marston, Phys. Rev. B **43** (1991), 2863.
- [50] M. Tinkham, *Introduction to superconductivity*, McGraw-Hill, New York, 1996.
- [51] J.M. Tranquada et al., Nature **375** (1995), 561.

- [52] U. Welp et al., Phys. Rev. Lett. **76** (1996), 4809.
- [53] X. Wen and P.A. Lee, Phys. Rev. Lett. **76** (1996), 503.
- [54] J.C. Wynn et al., Phys. Rev. Lett. **87** (2001), 197002.
- [55] N. Nagosa Y. Tokura, Science **288** (2000), 462.
- [56] E. Zeldov and others., Nature (London) **375** (1995), 373.
- [57] S.C. Zhang, Science **275** (1997), 1089.